EPSC2017

TP7 abstracts

EPSC Abstracts
Vol. 11, EPSC2017-26, 2017
European Planetary Science Congress 2017

Thermal radiation from large bolides and impact plumes

V. Svetsov and V. Shuvalov
Institute for Dynamics of Geospheres RAS, Moscow, Russia (svettsov07@rambler.ru / Fax: +7-499-1376511)

Abstract

We have carried out numerical simulations of the impacts of asteroids and comets from 20 m to 3 km in diameter and calculated thermal radiation fluxes on the ground and luminous efficiencies. 50-m-diameter bodies can ignite forest fires within a radius of up to 40 km and 3-km asteroids – within 1700 km.

1. Introduction

Direct thermal radiation from superbolides or impact plumes can ignite fires over large areas: 200-500 km^2 in the case of the 1908 Tunguska airblast [e.g., 1] and 3-5% of the total Earth's surface in the Chicxulub impact event [2]. Thermal radiation damage in a general case can be estimated using an analogy with nuclear explosions and some values of luminous efficiency of hypervelocity impacts [3]. However, the luminous efficiency (fraction of impactor kinetic energy emitted as thermal radiation) is not well constrained and fireballs and impact plumes can significantly differ in shape and energy from nuclear explosions. Asteroid and comet hazards demand assessments that are more accurate, but determination of radiation intensity presents a problem associated with a great amount of computations.

2. Numerical technique

The simulations of impacts were carried out using a hydrodynamic model, equations, and a numerical technique described, e.g., in [4]. We assumed that the cosmic object has no strength, deforms, fragments, and vaporizes in the atmosphere. After the impact on the ground, formation of craters and plumes was simulated taking into account internal friction of destroyed rocks and a wake formed in the atmosphere. The equations of radiative transfer, added to the equations of gas dynamics, were used in the approximation of radiative heat diffusion or, if the Rosseland optical depth of a radiating volume of gas and vapor was less than unity, in the approximation of volume emission. We used temperature and density distributions obtained in the simulations to calculate radiation fluxes on the Earth's surface by integrating the equation of radiative transfer along rays passing through a luminous area. We used tables of the equation of state of dunite, quartz (for impactor and target) and air, and tables of absorption coefficients of ordinary chondrite vapor and air (see refs. in [4]).

3. Results of numerical simulations

In the case of the 2013 Chelyabinsk superbolide (20-m-diameter asteroid, entry angle to horizontal θ=19°), the maximum radiation flux on the ground is about 2.5 W/cm^2 and the maximum radiant exposure (thermal energy incident on a unit area) is about 3 J/cm^2, which is insufficient for palpable skin burns but can cause temporal flash blindness in agreement with the eyewitness reports. The calculated luminous efficiency η is 17%. For rough estimates one can use the approximation of a point light source located at an altitude of 30 km, however, at distances about 100 km from the point with maximum irradiation on the ground the radiant exposures can substantially differ, up to two times. Numerical simulations of an airburst caused by a 50-m-diameter stony asteroid (dunite, density 3.3 g/cm^3) entering the atmosphere at an angle of 45° with a velocity of 20 km/s (kinetic energy 10.4 Mt TNT) gave an altitude of an airburst about 10 km, η=3.5%, and an area of forest ignition (deciduous leaves or rotted wood) about 350 km^2, quite similar to the 1908 Tunguska event.

A series of simulations of bolides show that η grows if the body diameter D and the entry angle θ decrease. For a stony 30-m-diameter asteroid entering the atmosphere at 20 km/s η=19% if θ=15° and η=4.5% if θ=90°. For D=50 m η=14.5% if θ=15° and η=2.6% if θ=90°. For cometary bodies (water ice, density 1 g/cm^3) of the same sizes η is from 1.5 to 3 times bigger than for the stony bodies. The bodies with a diameter of 30 m do not carry a risk of fire, but 50-m-diameter bodies can ignite fires in areas with radii from 10 to 40 km, depending on their velocity. Bodies with D=100 m can produce fires within a radius of up to 100 km.

If an asteroid hits the ground, the main source of radiation is vaporized material of an asteroid and a target in the impact plume. The vapor heated to temperatures 2000-2500 K reaches heights about 300 km if D=1km (Fig. 1) and above 600 km if D=3 km. In contrast to bolides, luminous efficiency decreases with decreasing θ because for smaller θ less energy is transferred to the impact plume. E.g., for D=1 km η=13% if θ=60° and η=8% if θ=30°.

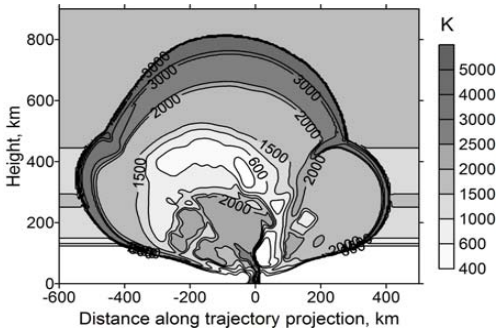

Figure 1: Isotherms in the atmosphere 80 s after the impact of a 1-km-diameter stony asteroid that entered the atmosphere at 45° with a velocity of 20 km/s and moved from right to left. The outer contour lines with temperatures above 3000 K correspond to a shock wave that accelerates upward but radiates only slightly because of a very low density of air.

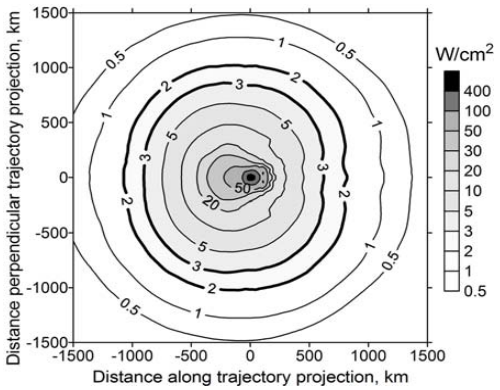

Figure 2: Contour lines of maximum radiation flux densities on the Earth's surface calculated for the impact shown in Fig. 1. It was assumed that atmospheric visibility is 30 km.

Duration of a thermal pulse from its beginning to its maximum τ is 100-150 s if D=1 km, in this case dry leaf litters can be ignited if maximum radiation flux density Q is 2-3 W/cm^2 [5]. As shown in Fig. 2, the average radius R of the area of potential fire ignition is 800-1000 km. If D=3 km, τ =200-250 s and live pine needles are ignited at Q~3-4 W/cm^2, R~1700 km.

4. Conclusions

Direct thermal radiation from fireballs and impact plumes produced by asteroids and comets larger than 50 m in diameter is dangerous for people, animals, plants, economic objects. Fires can be ignited on the ground within a radius of roughly 1000 times the body's diameter (for D≤1 km), and melted rocks could be found around impact craters on the Earth and terrestrial planets. During the Phanerozoic 1-km-diameter asteroids (that fall once in 1 My) could left about 500 craters with the traces of thermal radiation.

Acknowledgements

The work was supported by Russian Science Foundation, grant 16-17-00107. The authors are grateful to I. Kosarev for providing absorption coefficients of LL-chondrite vapor.

References

[1] Svetsov, V.V.: Comment on "Extraterrestrial impacts and wildfires", Palaeogeogr. Palaeoclimatol. Palaeoecol., Vol. 185, pp. 403-405, 2002.

[2] Shuvalov, V.V.: Radiation effects of the Chicxulub impact event, Geological and Biological Effects of Impact Events, pp. 237-247, Springer-Verlag, New York, 2002.

[3] Collins, G.S., Melosh, H.J., and Marcus, R.A.: Earth Impact Effect Program: A Web-based computer program for calculating the regional environmental consequences of a meteoroid impact on Earth, Meteoritics & Planetary Science, Vol. 40, pp. 817-840, 2005.

[4] Shuvalov, V.V., Svettsov, V.V., Artem'eva, N.A., Trubetskaya, I.A., Popova, O.P., and Glazachev, D.O.: Asteroid Apophis: Evaluating the impact hazards of such bodies, Sol. Sys. Res., Vol. 51, pp. 44-58, 2017.

[5] Belcher, C.M., Hadden, R.M., Rein, G., Morgan, J.V., Artemieva, N., and Goldin, T.: An experimental assessment of the ignition of forest fuels by the thermal pulse generated by the Cretaceous-Palaeogene impact at Chicxulub, J. Geol. Soc., Vol. 172, pp. 175-185, 2015.

EPSC Abstracts
Vol. 11, EPSC2017-33, 2017
European Planetary Science Congress 2017

Resurge deposits supporting a marine target of the Early Cambrian Vakkejokk impact, north Sweden

J. Ormö (1), P. Minde (2), A.T. Nielsen (3) and C. Alwmark (4)
(1) Centro de Astrobiología (INTA-CSIC), Spain (ormoj@cab.inta-csic.es), (2) Stockholm University, Sweden, (3) University of Copenhagen, Denmark, (4) Lund University, Sweden.

Abstract

The 520 Ma Vakkejokk Breccia, Sweden, likely is a proximal ejecta layer from an impact in a marine environment. Three short core drillings give evidence for resurge deposits supporting a marine target.

1. Introduction and aim of study

The ⩽27m thick Vakkejokk Breccia (VB) is semi-continuously exposed for a stretch of about 7km. Recent studies, including the discovery of planar deformation features in quartz (PDF) suggest the breccia to be impact related [1]. The VB is intercalated in a shallow marine succession that was deposited after the peneplanized Precambrian basement was transgressed in the Early Cambrian. The autochthonous sequence begins with the ~5m thick, transgressive, Lower Sandstone member, followed by the ~20m thick Lower Siltstone member (It is this unit that in the study area is partially replaced by the VB), which is in turn abruptly overlain by the 15-25m thick Red and Green Siltstone member. All together this suggests a marine target setting for the inferred impact. Based on sequence stratigraphical reasoning the VB is correlated to an absolute age of ≈520Ma [1]. The crater is estimated to be 2-3km wide, and most likely located below nearby Caledonian overthrusts [1].

The lower part of the VB is characterized by highly disturbed sandstone and siltstone blocks intermingled with clasts deriving from the Precambrian basement, some of decameter dimensions. This sub-unit is referred to as the 'lower polymict breccia' (LPB), and is suggested to have formed by ballistic bombardment of the sedimentary strata surrounding the crater by crystalline basement ejecta [1]. Overlying the LPB with a usually rapid transition is a polymict breccia, most commonly meter-thick and often graded. It occurs as both matrix-supported (most commonly a green, but also red-brown, silt), and as clast-supported, often in the upper half. Grading is obvious in the clast-supported variety, but occurs in the matrix-supported part as well, and thus this subunit is called 'graded polymict breccia' (GPB) [1]. It is at some sites overlain by an up to a few dm thick bed of quartzitic sand ('top sandstone', TS). It is from the GPB and TS that grains of shocked quartz have been retrieved [1]. These sub-units are suggested to have formed by marine resurge carrying ejecta and rip-up material back towards the crater. Locally the TS seems to be replaced by a mostly matrix-supported conglomerate that is suggested to originate from later slumps associated with degradation of the crater rim [1].

It is known from marine-target craters such as Lockne, Tvären, and Chesapeake Bay that the resurge deposits are essential for disentangling the marine cratering process and estimating target water depth [e.g., 2, 3]. Nevertheless, in the usually weathered exposures of the VB it is not always easy to see the sedimentological relations between the putative resurge deposits and underlying para-autochthonous breccia, notably whether there are gradual transitions, or erosive boundaries. This is more readily investigated in drill-cores.

2. Methods

Based on the previous mapping by Ormö et al. [1] three drill sites were selected that display a succession of TS and GPB overlying the para-authochtonous LPB. The first core, Vakk-CH1, was retrieved at N68° 22.259', E19° 14.132'. The other two cores, Vakk-CH2A&B, were drilled a further 100m to the west and only 1.5m apart at N68° 22.269', E19° 14.013' (Fig. 1). The cores were cut into halves. One half was polished to allow detailed visual logging and high-res photos. A first granulometric log was made by applying the line-logging technique given by Ormö et al. [2, 3] in which clast lithology and size (⩾ 5mm) was determined.

Figure 1. Drilling of Vakk-CH2B with a HILTI DD-200 (52mm drill crown)

As the short cores do not allow the statistical treatment of clast granulometry per meter, the line-logging results are seen as indicative, but also as a guide for the statistically more relevant logging carried out with the software JMicroVision v1.2.7. Here, a preset box of 20cm^2 was systematically moved along the core photos. The box area is chosen so that to obtain an amount of clasts similar to that of published line-logs [i.e., 3]. The box width is set to fill up the width of the core with some margin. In case the core is very uneven in shape the box shape is adapted to the core maintaining the 20cm^2 surface area (In this study at only one location). The maximum length of the box is limited to locations with rapid changes in the sediment; The data is plotted at the depth of the center of the box (i.e., the shorter the box the narrower the data point spacing). Every clast $\geqslant$5mm inside the box is determined for size (visible length axis) and lithology. The exterior of the box is considered unknown, thus only the visible part of clasts crossing the perimeter of the box is measured. The outline of each clast is hand drawn allowing the percentage of matrix to be calculated by subtracting the total area of the clasts from the box area. Clast sizes are given as mean $-\Phi$ values per box (here called φ), and sorting is determined by the standard deviation (σ) of this value [cf. 2, 3].

3. Results and discussion

The three cores Vakk_CH1 (135cm), CH2A (85cm), and CH2B (135cm) show similar trends and due to limited space we here only describe Vakk_CH1; Notable is how: 1) There is an approximately 40cm thick graded arenite that has a gradual, although rapid, downwards transition to a clast supported breccia. This has a likewise gradual transition into a matrix-supported breccia towards the end of the core. 2) Siltstone clasts are generally larger than granite clasts at the same depth (i.e., transport energy in suspension), possibly as a result of their shape. 3) The clast-supported part is dominated by another variety of granite than the matrix-supported part. 4) The number of clasts is (logically) the highest in the clast-supported part. 5) Clast size varies greatly below 112cm depth. Above that level there is a slight fining-up trend, as well as a higher amount of crystalline (basement) clasts. 6) Sorting is improving upwards, indicating waning resurge flow [cf. 2, 3]. 7) Crystalline clasts dominate (especially above 112cm), but are upwards more and more replaced by (more easily transported?) siltstone clasts.

4. Conclusions

Although the data set is limited it shows systematic trends that we find support the model by Ormö et al. [2017] of a resurge of water and ejecta separated in an overriding hyperconcentrated suspension flow that drives a traction flow of ejecta and rip-up material from the underlying ballistic ejecta (LPB) (Fig. 2).

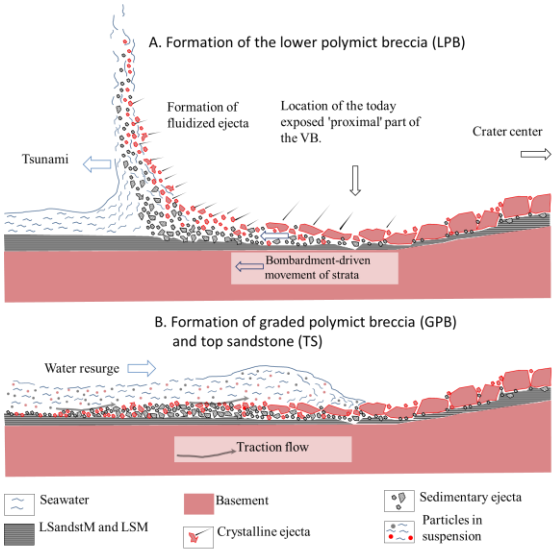

Figure 2. Model of formation of the VB with the para-autochthonous LPB and the subsequent resurge deposits GPB and TS. Modified from [1].

References

[1] Ormö, J., Nielsen, A. T., and Alwmark, C.: Meteoritics and Planetary Science, Vol. 52(4), pp. 623–645. 2017.

[2] Ormö, J., Sturkell, E., and Lindström, M.: Meteoritics and Planetary Science, Vol. 42(11), pp. 1929-1944, 2007.

[3] Ormö, J., Sturkell, E., Horton, J.W., Jr., Powars, D.S., and Edwards, L.E.: Geological Society of America Special Papers, Vol. 458, pp. 617-632, 2009.

EPSC Abstracts
Vol. 11, EPSC2017-66, 2017
European Planetary Science Congress 2017

2D Models for the evolving distribution of impact melt at the lunar near-surface

T. Liu (1,2), G. G. Michael (2) and J. Oberst (1,3)
(1) Institute of Geodesy and Geoinformation Science, Technical University Berlin, Straße des 17 Juni 135 Juni 135, H12, Berlin 10623, Germany (tiantian.liu@tu-berlin.de), (2) Planetary Sciences and Remote Sensing, Freie Universitaet Berlin, Malteser Strasse 74-100, Haus D, Berlin 12249, Germany, (3) Deutsches Zentrum für Luft- und Raumfahrt (DLR), Institute of Planetary Research, Rutherfordstrasse 2, D 12489 Berlin, Germany.

1. Introduction

Impact events have been the primary mechanism for modification of the lunar surface since the formation of the lunar crust [1]. Impacts produce varying amounts of melt, which may be identified and radiometrically dated in surface samples. Existing melt can be redistributed by the ejection process of subsequent impacts.

It is possible to evaluate the amount of the impact melts, but the cumulative effect of the impact gardening process (i.e. excavating, burying, and re-excavating) has not been systematically studied. Michael et al. 2014 simulated such long-term process by using the Monte Carlo method [2]. Nevertheless, the corresponding results are in an average sense, where the impact melt is considered to be evenly distributed over the entire lunar surface.

The purpose of this work is to refine the average model into two-dimension (2D) where the lateral distribution of impact melt is recorded, and the age of melts within the evolving mixture is tracked.

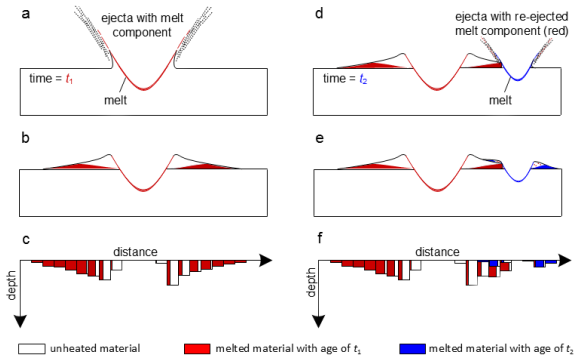

Figure 1. Schematic of the simulations. (a) Impact event causing ejecta of both unheated and melted material when time is t_1. (b) The deposition of ejecta with a mixed layer of unheated (white) and melted (red) material. (c) The expected lateral distribution of (b) in this model tracking the percent of unheated and melted material, the age of impact melt and the thickness of ejecta. (d) A subsequent impact event when time is t_2, penetrating the previous ejecta blanket, excavating material from both the previous layer and beneath, and melting a fraction of both (blue). (e) The deposition of a new layer containing both new melt and a component of re-excavated melt from the previous event. A fraction of ejecta materials overlay the previous deposition. (f) The expected lateral distribution of (e) in this model tracking the percent of unheated, melted material, the age of each fraction and the thickness of ejecta.

2. Method

The essence of the model is the following:

1. The minimum crater diameter considered, D_{min}, is chosen as 5 km based on the performance of computers.
2. By using the Monte Carlo method, the diameter of the formed craters is generated to conform to the production function larger than D_{min} [3].
3. The impact rate is calculated for the current model time, t, on the basis of the lunar chronology function, which describes the cumulative number of craters larger than 1 km in diameter at age t [3]. Using the production function the formation rate of craters larger than D_{min} is found.
4. The average time to the next impact event can be obtained based on the impact rate.
5. For each crater, the excavation depth is taken as $D/10$ [4], where D is the corresponding crater diameter.
6. The ejecta blanket thickness is related to the distance from crater center, r: $\delta = aR^b(r/R)^c$ for $r>R$, where R is the crater radius, and a, b, and c are taken as 0.14, 0.74 and -3.0, respectively [4].
7. The distribution of impact melt both inside and outside the crater has not been fully understood limited by the laboratory conditions or/and computer performance in the previous researches [5]. Such issue is under study in collaboration with the group guided by Kai Wünnemann. In this model, the power law normalization is performed for the melt in the ejecta, and assume

that 75% volume of the total melt would remain inside the crater.

The expected results after the lunar surface experiencing two impact events in this model are shown in Figure 1.

3. Results

A band of width 110 km passing along the great circle through the late-forming Imbrium basins, Serenitatis basin, and Crisium basin is chosen for modelling. Based on the crater statistics results, N(20), the ages of three basins are taken to be 3.88, 4.13, and 4.09 Ga, respectively [3, 6]. As the preliminary 2D model, only 1550 impact events on the great circle are considered, assuming the age of Serenitatis crater as the starting time.

Figure 2 shows the present day distribution of the impact melt at the lunar near-surface (~3.5 m). It can be seen that the melt of relatively young Imbrium basin and Crisium basin is dominant, comparing with that of Serenitatis basin. The melt of Imbrium basin is widespread. The melt younger than ~3.5 Ga locally distribute and is much less than the older one.

4. Conclusions and Future Work

The lateral distribution of the melt with diverse ages is traced in this model. Using the observed distribution of melt age in lunar samples and meteorites, the possible scenarios of the lunar impact history can be discriminated [2]. The record is also helpful for the future lunar sampling, guiding the choice of site to obtain samples from different impact basins, and to understand the mixture of melt ages observed at any one site.

There has long been a dispute over the cause of the high percent of lunar samples with age of ~3.9 Ga [7]. Some believe that it results from the impact cataclysm [8]. Others argue that it might be due to the origin of the collected samples, most of which might be the ejecta materials from Imbrium crater [7]. Our model shows that the melt of Imbrium basin is widespread. Is it possible that the melt is globally distributed? To find the possible distribution of the melt of Imbrium basin, the model need to be refined in the future work.

Acknowledgements

The work was supported by the German Research Foundation (DFG) SFB TRR-170-1 TP A4.

References

[1] Heiken, G. H., Vaniman, D. T., and French, B. M.: Lunar Source-Book: A User's Guide to the Moon, Cambridge Univ. Press, 1991.

[2] Michael, G. G.: Evolution of the presence of impact melt at the nearsurface of the Moon, EPSC2014-764, 2014.

[3] Neukum, G.: Meteoritenbombardement und Datierung planetarer Oberflächen, Dissertation for Faculty Membership, 186p, 1983.

[4] Melosh, H. J.: Impact cratering: a geologic process, Oxford Univ. Press, 1989.

[5] Personal communication with Kai Wünnemann (Museum für Naturkunde, Leibniz Institute for Evolution and Biodiversity Science, Berlin, Germany).

[6] Fassett, C. I., Head, J. W., Kadish, S. J. et al.: Lunar impact basins: Stratigraphy, sequence and ages from superposed impact crater populations measured from Lunar Orbiter Laser Altimeter (LOLA) data, Journal of Geophysical Research: Planets, 117(E12), 2012.

[7] Spudis, P., and Pieters, C.: Global and regional data about the Moon, In Lunar sourcebook, Cambridge Univ. Press, 595–632, 1991.

[8] Cohen, B. A., Swindle, T. D., and Kring, D. A.: Support for the lunar cataclysm hypothesis from lunar meteorite impact melt ages, Science, 290(5497), 1754-1756, 2000.

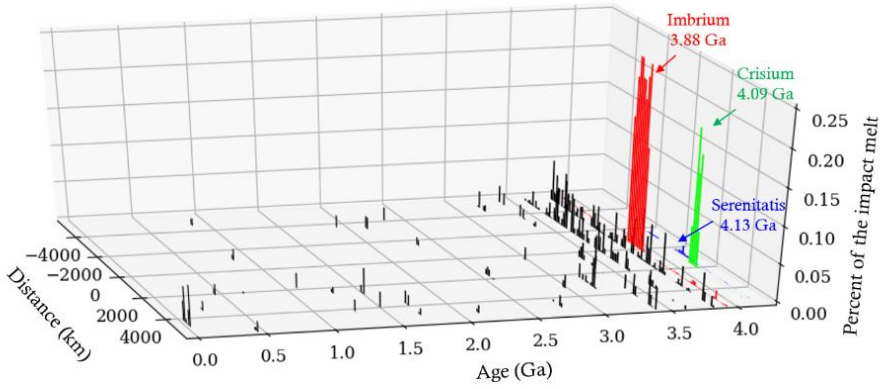

Figure 2. The present day distribution of the impact melt on the lunar near-surface

EPSC Abstracts
Vol. 11, EPSC2017-76, 2017
European Planetary Science Congress 2017

The martian moons as the remnants of a giant impact

T. Ronnet (1), P. Vernazza (1), O. Mousis (1), B. Brugger (1), P. Beck (2), B. Devouard (3), O. Witasse (4), F. Cipriani (4)
(1) Aix Marseille Univ, CNRS, LAM, Laboratoire d'Astrophysique de Marseille, Marseille, France (thomas.ronnet@lam.fr), (2) Univ. Grenoble Alpes, IPAG, F-38000 Grenoble, France, (3) Aix-Marseille Univ, CNRS, IRD, CEREGE, Aix en Provence, France, (4) European Space Agency, ESTEC, Keplerlaan 1, 2200 AG Noordwijk, The Netherlands

Abstract

The origin of Phobos and Deimos is still an open question. Currently, none of the three proposed scenarios for their origin (intact capture of two distinct outer solar system small bodies, co-accretion with Mars, and accretion within an impact-generated disk) is able to reconcile their orbital and physical properties. Here we show that gas-to-solid condensation of the building blocks in the outer part of an extended impact-generated disk could reproduce the spectral and physical properties of the moons.

1. Introduction

The present low eccentricity, low inclinations and prograde orbits of Phobos and Deimos are very unlikely to have been produced following capture [1] (see panel a in Fig. 1), thus favoring a formation of the moons around Mars (i.e., co-accretion with the planet or accretion in an impact-generated disk) [3, 5]. Despite such early robust evidence against a capture scenario, the fact that the moons share similar physical properties (low albedo, red and featureless VNIR reflectance, low density) with outer main belt D-type asteroids has maintained the capture scenario alive [4, 6]. Co-accretion with Mars appears unlikely because Phobos and Deimos would consist of the same building block materials from which Mars once accreted which are spectrally incompatible with the martian moons (see panel b in Fig. 1). Recently, a detailed study demonstrated how Phobos, whose distance to Mars is decaying due to tidal forces, could have survived since its formation within an impact-generated disk, asserting the strength of the scenario [7]. Although the impact scenario has become really attractive, it has not yet been demonstrated that it can explain the physical properties and spectral characteristics of the martian moons. We therefore investigated the mineralogical composition and texture of the dust that would have crystallized in an impact-generated accretion disk. We show that under specific disk's pressure and temperature conditions, Phobos and Deimos' physical and orbital properties can be finally reconciled.

2. Methods and Results

We considered various impact-generated disk chemical compositions as both the nature of the object that would have impacted Mars and the relative proportions of the impactor's mantle and Mars' mantle that would end up in the debris disk are unknown. More precisely we considered disks with a Bulk Silicate Mars, Bulk Silicate Moon and Interplanetary Dust Particle chemical compositions. We used a normative calculation (CIPW norm calculation) to infer the mineralogical composition of the solids that would cristallize from such disks. The cooling timescales of the disk and the clumps that would form from the magma layer in the midplane were estimated to determine the size range (i.e., texture) of the grains that would crystallize. We find that olivine and pyroxene are likely to be the major crystallized minerals for each composition considered. The grains that would crystallize from the molten midplane layer would typically fall into the 0.1–1 mm size range. Such minerals have well defined absorption bands that would be clearly identifiable in the spectra of Phobos and Deimos. These findings disagree with the observed featureless spectra of both moons (Fig. 1 panel c-left).

3. Discussion

Our study preclude the formation of Phobos and Deimos from a molten disk that would spread and form clumps while crossing the Roche limit ($\sim$4 R_{Mars}), similarly to the processes that gave birth to the Moon [2]. However, the temperature and pressure conditions in the extended disk (in the vicinity of the synchronous orbit at $\sim$6 R_{Mars}) are likely to allow the direct condensation of the vapor into solid grains. Laboratory experiments show that the condensation

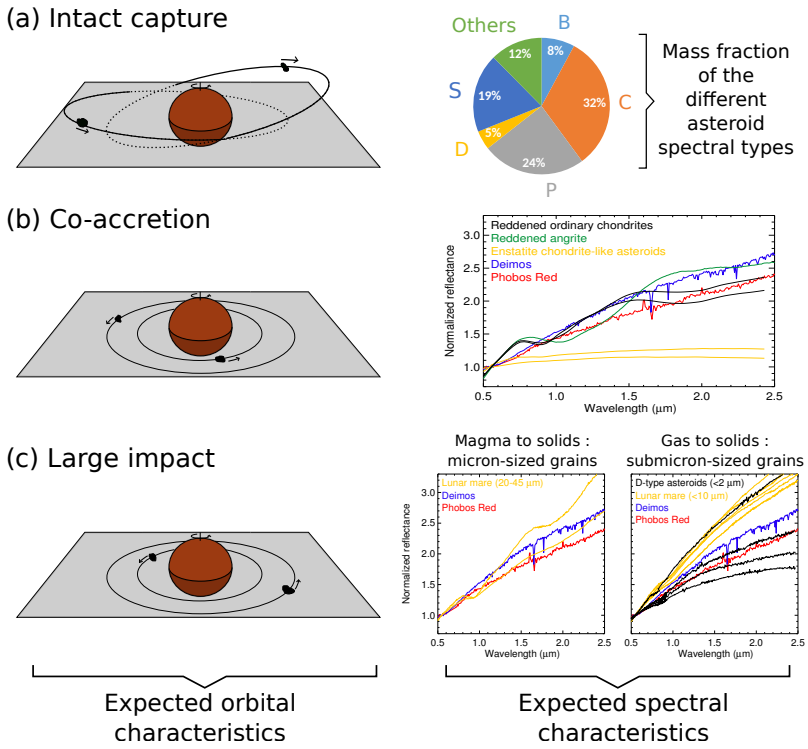

Figure 1: Schematic representation of the expected orbital (left) and spectral (right) characteristics of the martian moons for each of the three different scenarios currently invoked for their origin.

of a silicate vapor results in very fine dust grains, with typical sizes of 0.1 microns [8]. Recent studies have shown that a space weathered mixture of sub-micron sized olivine and pyroxene grains would possess spectral properties similar to those of P- and D-type asteroids [9]. The formation of Phobos and Deimos in a low-pressure extended disk would therefore naturally results in objects whith spectral properties very close to those of these primitive asteroids (panel c-right of Fig. 1). This conclusion is in agreement with a recent dynamical study demonstrating that the formation of Phobos and Deimos should have occured in the extended debris disk to account for their current orbits [7].

P.V. and O.M. acknowledge support from CNES. This work has been partly carried out thanks to the support of the A*MIDEX project (n° ANR-11-IDEX-0001-02) funded by the "Investissements d'Avenir" French Government program, managed by the French National Research Agency (ANR).

References

[1] Burns, J. A. 1978, VA, 22, 193

[2] Canup, R. M., Visscher, C., Salmon, J., & Fegley, B. Jr. 2015, NatGe, 8, 918

[3] Cazenave, A., Dobrovolskis, A., & Lago, B. 1980, Icar, 44, 730

[4] Fraeman, A. A., Murchie, S. L., Arvidson, R. E., et al. 2014, Icarus, 229, 196

[5] Goldreich, P. 1963, MNRAS, 126, 257

[6] Pajola, M., Lazzarin, M., Dalle Ore, C. M., Cruikshank, D. P., Roush, T. L., Magrin, S., Bertini, I., La Forgia, F., & Barbieri, C. 2013, ApJ, 777, 127

[7] Rosenblatt, P., Charnoz, S., Dunseath, K. M., et al. 2016, Nature Geoscience, 9, 581

[8] Toppani, A., Libourel, G., Robert, F., & Ghanbaja, J. 2006, Geochim. Cosmochim. Acta, 70, 5035

[9] Vernazza, P., Marsset, M., Beck, P., et al. 2015, ApJ, 806, 204

EPSC Abstracts
Vol. 11, EPSC2017-182, 2017
European Planetary Science Congress 2017

Simulation of ejecta–atmosphere interaction

R. Luther (1), N. Artemieva (2,3) and K. Wünnemann (1)
(1) Museum für Naturkunde Berlin, Leibniz Institute for Evolution and Biodiversity Science, (2) Planetary Science Institute, Tucson, USA, (3) Institute for Dynamics of Geospheres, RAS, Russia (robert.luther@mfn-berlin.de)

Abstract

We study the interaction of ejected material from impact craters with an atmosphere or an impact induced vapour phase. This interaction depends on the size distribution of ejected particles.

1. Introduction

The ejection of material during impact cratering is an important process that is relevant for various aspects. In our study, we focus on the deposition of ejecta and the formation of an ejecta blanket. The initial characteristics of ejecta (launch velocity and ejection angle) have been shown to depend on target properties (e.g. strength and porosity; see e.g., [1-3]). Based on these characteristics, ejecta trajectories can be calculated in vacuum as parabolas. However, in the presence of an atmosphere, ejection trajectories deviate from pure ballistic trajectories and the final deposition will be different from vacuum conditions [e.g. 4]. In this study, we present numerical results of ejecta interaction with an atmosphere.

2. Method

We use the iSALE shock physics code [5-7] to simulate the behaviour of ejected material in contact with gas from an atmosphere. The strengths of iSALE are the availability of: (1) different material models (brittle/ductile rheology), (2) a damage model, (3) various equations of state, and (4) a porosity compaction model. Having been used mostly for the simulation of crater formation in dense materials, iSALE has been applied recently to the simulation of shock events in an atmosphere [8]. In order to simulate the interaction of ejected particles with an atmosphere, we added a dusty flow model [9-11]. Therefore, we transform material from a cell (continuum behaviour in a grid) into representative particles once ejection (transformation) criteria are fulfilled [10-11]. Representative particles are characterized by a velocity, shape and size. Two main forces act on the ejected particles: gravity, and drag by the surrounding gaseous medium:

$$m\frac{dv}{dt} = m\boldsymbol{g} + C_D\pi r^2\rho_g|\boldsymbol{v}_g - \boldsymbol{v}|(\boldsymbol{v}_g - \boldsymbol{v}) + 6\pi r\mu(\boldsymbol{v}_g - \boldsymbol{v}), \quad (1)$$

where C_D is the drag coefficient, g the gravitational acceleration, m and r the particle mass and radius, ρ_g and μ are gas density and viscosity, and $\boldsymbol{v}$ and $\boldsymbol{v}_g$ are the particle and gas velocity. Representative particles also exchange energy and momentum with the surrounding gas/vapour. We use an ideal gas as equation of state with a surface density of ~1kg/m³.

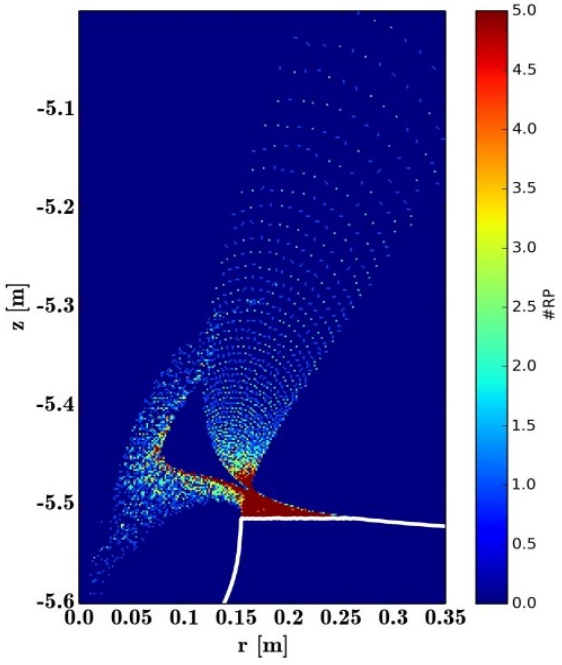

Figure 1: Representative particles (10 µm and 1 cm in size) are ejected from a forming crater cavity. Both size classes separate from each other by atmospheric interaction. Small particles are affected by a gas flow into the cavity. Note, that due to the different sizes of particles, the colour scale is not equivalent to the mass of each representative particle. The impact velocity is 4.5 km/s.

3. Preliminary Results

In a first series, we simulate the movement of representative particles in a static atmosphere and analyse the trajectory of representative particles of different sizes. Particle-gas-interaction is size dependent (eq. 1) and small particles experience more gaseous drag and are decelerated faster than larger fragments. However, when particles of two size classes move along a trajectory at the same time, the larger particle will influence the atmosphere in such a way that smaller particles can travel further relative to a scenario where larger particles are absent; i.e. large particles increase the velocity of the gaseous medium, reducing relative velocities for the smaller particles and the gas (eq. 1), leading to a reduced deceleration of the smaller particles.

In a second series, we simulate an impact into a target, where representative particles are created by transforming material from the grid as described above. We use different particle sizes in different runs, ranging from 10 μm to 1 cm. We also run a simulation with both 10 μm and 1 cm sized particles (Figure 1). We see a separation of particles according to their size. Small particles are engaged in a gas flow into the expanding cavity.

4. Discussion

Our results show that the interaction of ejecta and an atmosphere cannot be neglected. It causes ejection trajectories that differ significantly from pure ballistics trajectories. Thus, ejecta deposition will be different and a layering according to particle size is possible. Furthermore, depending on the size distribution of particles and wind fields, small dust particles can be moved to various positions including the crater cavity. Especially trajectories of dust particles are crucial for estimating the climatic effects of large impact event [e.g., 12].

Acknowledgements

We thank the developers of iSALE, vimod and pySALEPlot. This work was funded by DFG as part of MEMIN FOR887, WU 355/6-2 and the SFB-TRR170 A4.

References

[1] Collins, G. S., and Wünnemann, K.: The effect of porosity and friction on ejection processes: Insight from numerical modeling, Bridging the Gap II, 22.-26. September 2007, Saint-Hubert, Canada, LPI Contribution No. 1360, p.35-36, 2007.

[2] Housen, K. R. and Holsapple, K. A.: Ejecta from impact craters, Icarus 211, pp. 856-875, 2011.

[3] Luther, R., Artemieva, N. A., Collins, G. S., and Wünnemann, K.: Impact Ejecta Mechanics: Influence of Target Properties and Atmospheric Interaction on Ejecta, 48th LPSC, 20.-24. March 2017, The Woodlands, USA, LPI Contribution No. 1964, id.1942, 2017.

[4] Shuvalov, V. V. and Dypvik, H.: Distribution of ejecta from small impact craters, Meteorit. & Planet. Sci. 48, pp. 1034-1042, 2013.

[5] Amsden A., Ruppel, H. M., and Hirt, C. W. : Sale : A Simplified ALE Computer program for Fluid Flow at All Speeds, LANL, LA-8095, 101, 1980.

[6] Collins, G. S., Melosh, H. J., and Ivanov, B. A.: Modeling damage and deformation in impact simulations, Meteorit. & Planet. Sci. 39, pp. 217-231, 2004.

[7] Wünnemann, K., Collins, G. S., and Melosh, H. J.: A strain-based porosity model for use in hydrocode simulations of impacts and implications for transient crater growth in porous targets, Icarus 180, pp. 514-527, 2006.

[8] Collins, G. S., Lynch, E., McAdam, R., and Davison, T.: A numerical assessment of simple airblast models of impact airbursts, Meteorit. & Planet. Sci., 2017.

[9] Shuvalov, V. V.: Multi-dimensional hydrodynamic code SOVA for interfacial flows: Application to the thermal layer effect, Shock Waves 9, pp. 381-390, 1999.

[10] Artemieva, N. A. and Ivanov, B. A.: Launch of martian meteorites in oblique impacts, Icarus 171, pp. 84-101, 2004.

[11] Artemieva, N. A., Wünnemann, K., Krien, F., Reimold, W. U., and Stöffler, D.: Ries crater and suevite revisited-Observations and modelling, Meteorit. & Planet. Sci. 48, pp. 590-627, 2013.

[12] Pierazzo, E., Kring, D. A., and Melosh, H. J.: Hydrocode simulation of the Chicxulub impact event and the production of climatically active gases, J. Geophys. Res. 103, pp. 28,607-28,625, 1998.

EPSC Abstracts
Vol. 11, EPSC2017-232, 2017
European Planetary Science Congress 2017

Impact-induced melting by giant collision events – Implications for the formation of magma oceans on terrestrial planets

L. Manske, K. Wünnemann, Museum für Naturkunde, Freie Universität Berlin, Invalidenstraße 43, 10115 Berlin, Deutschland (Lukas.Manske@MfN-Berlin.de)

Abstract

We revisit the longstanding problem how to estimate melt production during giant collision events, which may not be accurately addressed by classical scaling-laws. Therefor we carried out a series of numerical models of impact scenarios considering the initial temperature, the solidus, and the layered structure of planetary bodies.

1. Introduction

Giant collisions such as the Moon-forming event on the young Earth or basin-forming impacts are known to have influenced the chemical and thermal evolution of the terrestrial plants [4]. Besides the material that is delivered by such impacts, a significant amount of energy is transferred to the planet resulting in heating up its interior. Existing scaling-laws can predict the amount of shock melting [1,2,6] generated by impact events smaller than basin-forming events. On the scale of giant collisions such scaling laws may not be accurate as they do not account for the initial temperature and lithostatic pressure of planets interior. This can be particularly problematic for younger planets, where the initial temperatures are close to the given solidus. To better understand and quantify the mechanism of heat production and melting during large-scale impact events we conducted a series of numerical models and determined the volume of melt production.

2. Methods

To model hypervelocity collisions we use the iSALE Eulerian shock physics code [3,8] (Version *Dellen*). In iSALE the thermodynamic state (EoS) is calculated by look-up tables derived from ANEOS [eg. 5] for dunite, basalt, granite, and iron representing the Planets crust, mantle and core, respectively.

2.1 Melt calculation

To determine the distribution and volume of impact-induced melting we calculate the local increase of temperature $\Delta T(x,z)$ via the peak shock pressure method assuming that the temperature gain is directly proportional to the peak shock pressure [6]: Therefor massless Lagrangian tracers record the peak shock pressure and track their displacement during crater formation. Each tracer is associated with the mass of material in the cell, where the tracer was initially located in. The final Temperature of a tracer T_f is then determined by adding the shock-induced temperature increase $\Delta T(x,z)$ to the initial Temperature T_i: $T_f = T_i + \Delta T(x,z)$. By comparing T_f with the solidus temperature T_s=f(P_f), where f(P_f) is given by the Simon approximation [7] and P_f is the post-impact pressure at the final position of each tracer, we determine whether a “tracer” (the associated mass) is molten or not. By this approach we also account for decompression melting as a consequence of displacement of matter in the course of crater formation.

2.2 Model

For the different terrestrial planets we assume individual initial conditions regarding composition and temperature distributions, typical impact velocities, and gravity. Our planetary models include a dunitic mantle, and an iron core. For the impactor we also assume a dunitic composition. Differentiated bodies are neglected at this stage. In case of the Earth we use a setup according to the model described by Marchi et al. [2] that includes a granitic crust, while in the model of the Mars, the crust consists of basalt. We consider different thermal profiles (T_i=f(P)) representing different stages of the thermal evolution of a given planet. In all models the projectile radius is resolved by 50 cells (50 CPPR). For very large impacts we account for the curvature of the target.

3. Parameter study for impact-induced melting

In our systematic parameter study we vary impactor diameter L and velocity v_i for different temperature conditions on each planet. A reference model M_{REF} without the effects of gravity, material strength, and depth-dependent temperature, but with an earth-like layered target has been calculated, which can be directly compared with classical scaling-laws. Figure 1 shows that the reference model agrees with the scaling-laws. Depending on the impactor diameter L crust or mantle melting dominates. The more realistic model M_{Earth} (as discribed in 2.1) is approximately in agreement with classic scaling for smaller impacts; however, larger events are not well represented. It can be shown, that the different melt volumes of both models at lager impactor diameters primarily resulting from additional decompression melting in areas, where the solidus and the initial temperatures are close.

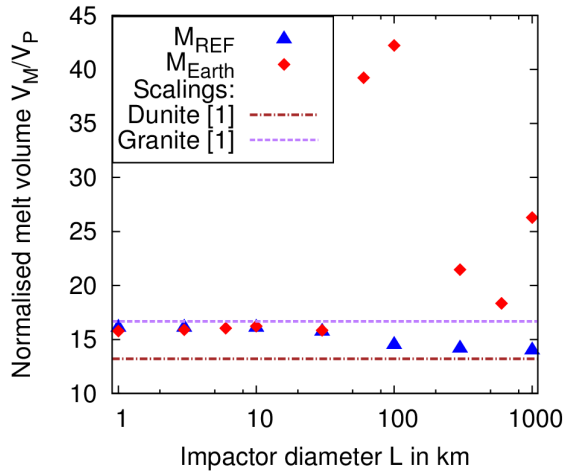

Figure 1: Normalised melt volume V_M by the projectile volume V_P as a function of impactor diameter L on an earth like planar target (red). The reference model (cf.Text) is indicated by a blue dots. The Impact velocity in both models v_i is 17 km/s. Similar behavioer can be observed for impact generated melting on Mars.

The goal is to derive a parameterization for the volume of impact-induced melting V_m as a function of impact parameters $V_m = f(L, v_i, T_i, P_f)$ for collision events arbitrary in scale.

Acknowledgements

We gratefully acknowledge the developers of iSALE, including Gareth Collins, Kai Wünnemann, Dirk Elbeshauesn, Boris Ivanov and Jay Melosh. This work was funded by the Deutsche Forschungsgemeinschaft (SFB-TRR 170, subproject C2 and C4).

References

[1] Abramov O. et al.: Differential melt scaling for oblique impacts on terrestrial planets, Icarus 218, 906-916, 2012.

[2] Bjorkman, M. D. and Holsapple K. A.: Velocity scaling impact melt volume, Int. J. Impact Eng. 5, 155–163, 1987.

[3] Collins. G. S. et al.: Modeling damage and deformation in impact simulations, Meteoritics & Planet. Sci. 39, 217-231, 2004

[4] Marchi S. et al.: Widespread mixing and burial of Earth's Hadean crust by asteroid impacts, Nature 511, 578-582, 2014.

[5] Melosh H. J.:A hydrocode equation of state for SiO_2, Meteoritics & Planet. Sci. 42, 2079-2098, 2007.

[6] Pierazzo et al.: A Reevaluation of Impact Melt Production, Icarus 127, 408-423, 1997.

[7] Poirier, J. P.: Introduction to the Physics of Earth Interior, Cambridge Univ. Press, 1991.

[8] Wünnemann K. et al.: A strain-based porosity model for use in hydrocode simulations of impacts and implications for transient crater growth in porous targets, Icarus 180, 514–527, 2006.

EPSC Abstracts
Vol. 11, EPSC2017-251-2, 2017
European Planetary Science Congress 2017

Quantification of shock-induced melting and its distribution in the Ejecta

J. Engelmann[1,2], K. Wünnemann[1], R. Luther[1], M.-H. Zhu[3], [1]Museum für Naturkunde, Leibniz Institute for Evolution and Biodiversity Science, Berlin, Germany (kai.wuennemann@mfn-berlin.de); [2]Freie Universität Berlin, Institute for Geological Sciences; [3]Space Science Institute, Macau University of Science and Technology, Macau.

Abstract

In contrast to lunar regolith, which is dominated by impact melt particles (agglutinates), samples from the asteroid Itokawa (25143), collected by the Hayabusa mission, exhibit a strong deficit in agglutinates. To investigate the amount of shock-induced melting and its distribution in the ejecta we simulate hypervelocity impacts into targets with varying gravity and quantify the amount and distribution of generated melt that is ejected. We find that even at relatively low impact velocities and high target porosity (representing asteroidal condition) a significant amount of melting occurs.

1. Introduction

The surfaces of atmosphereless bodies are subject to a continuous flux of impactors ranging from micro-meteoroids to large, crater-forming objects. Independent from the size-scale hypervelocity impacts generate shock waves that lead to distinct shock metamorphic effects in silicates including melting and the formation of amorphous glasses. On the Moon, impact gardening and space weathering have formed a regolith layer dominated by impact melt particles (agglutinates) [1]. The ejecta thickness on the Moon generally decreases with increasing distance from the crater. The regolith layer on the asteroid Itokawa (25143) directly sampled by the Hayabusa mission [2] shows a distinctly different picture: dust particles exhibit different (solid-state) shock features, but agglutinates appear to be rare. The deficit in impact melt in the Itokawa regolith may be explained in two ways: (1) the relatively low impact velocities on asteroids in comparison to the Moon generate shock pressures insufficient to cause melting; (2) the vast majority of impact generated melt is ejected and escapes the low gravity environment on asteroids. (1) can be ruled out as several studies have shown that shock melting and agglutinate-like particles occur in granular target material even at impact velocities as low as ~ 2.5 km s^{-1} [1,3,4]. This is because the high porosity in regolith reduces the critical pressure for shock melting significantly [5]. Here we investigate the second option, that most impact melt is ejected and escapes the low-gravity field. We compare the results for the conditions on an asteroid with the melt distribution in the ejecta for lunar conditions.

2. Methods

We use the iSALE shock-physics code [6] to simulate hypervelocity impact processes. In a first step we validated our model against laboratory experiments. In a second step we conducted a suite of impacts in a low gravity environment (Table 1). To account for target porosity and its effect on the reduction of the critical shock pressure required for melting we used the ε–α compaction model [6]. The amount of material that experienced a certain shock pressure was measured by recording the peak shock pressure with tracers.

Table 1: Model Setup

Model Type	Resolution (CPPR)	Impact velocity (kms^{-1})	Porosity (%)	Thermodyn. Behaviour (ANEOS)
Shock Vol.	10/20	2.5–12.5	0-60	Aluminum/ Quartz, Basalt [8,9]
Ejecta	60			

3. Results

Figure 3 shows the results of impact models in a low gravity regime (g = 0.0162 m s^{-2}). Note that gravity does not affect melt production and has little effect on the ejection mechanics. However, gravity effects

whether ejected material can escape the gravity field of an asteroid and the distribution of material expelled from a crater forming an ejecta blanket (e.g. on the Moon). To calculate the escape volume on an asteroid, we used the real escape velocity on Itokawa of ~ 0.2 m s^{-1}. We also verified that the amount of melt relative to the size of the impactor is constant. Figure 3 shows the percentage of melt that is ejected and escapes the gravity field (ejection velocity > escape velocity) as a function of impact velocity and target porosity. At zero porosity (brown line) no melt is generated at 5 km s^{-1}. At 7.5 km s^{-1} almost 70% of the generated melt escapes the gravity field. At higher velocities more melt is generated, but the relative amount of escaped melt decreases. In fact the vast majority of melt that does not escape the asteroid remains inside the crater and is not ejected. This is most likely due to the fact that we consider vertical impacts only, which is a limitation of the 2D cylindrical geometry in our models. Material that is highly shocked and located in a cone-shaped volume underneath the point of impact is displaced into the target, lining the crater wall as a thin veneer, but is not ejected. This may change significantly in case of more realistic oblique impacts. For porosities ⩾20%, melt is already generated at an impact velocity of 2.5-5 km s^{-1}, but the escape melt volume also decreases with increasing impact velocity.

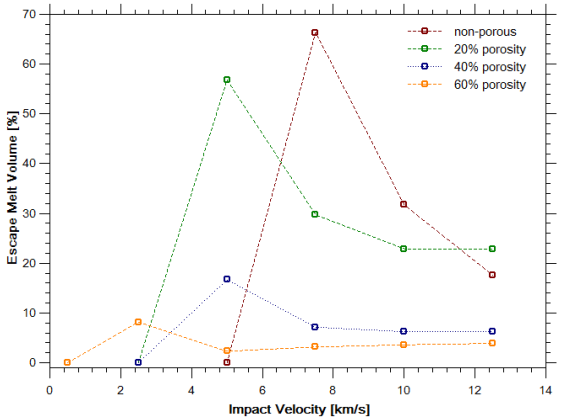

Figure 3: Percentage of melt that is ejected and escapes the gravity field of an Itokawa-like asteroid relative to the total amount of generated impact melt as a function of impact velocity. According to [7], we assume for the critical peak pressure for melting ~ 60, 30, 15, and 5 GPa for 0%, 20%, 40%, and 60% porosity, respectively. The projectile diameter is 50 m. We assumed a basalt ANEOS for both target and projectile.

4. Conclusions

Our models are in excellent agreement with observations from laboratory experiments, building high confidence in our results. Although our estimated critical shock pressures for melting of porous basalt may be questionable, different critical shock pressures would only cause a small shift of the lines shown in Figure 3. Given the fact that ejection dynamics change significantly in case of oblique impacts, the biggest limitation is the vertical impact simplification. Overall, our study demonstrates that a significant amount of melting occurs at relatively low impact velocities if the target is porous. Our models also predict that in case of vertical impacts a significant amount of the generated melt remains inside the crater and is not ejected. Currently, we are investigating the distribution of shock melting in the ejecta with increasing distance from the crater for impact scenarios that are typical on the Moon.

Acknowledgements

We acknowledge the developers of iSALE, VIMoD and pySALEPlot.

References

[1] Hörz F. et al. (2005) Meteorit. Planet. Sci., 40, 1329–1346.

[2] Nakamura T. et al. (2011) Science 333, 1113–1116.

[3] Daly R. T. & Schultz P. (2016) Icarus, 264, 9–19.

[4] Hamann C. et al. (2016) Geochim. Comsochim. Acta, 192, 295–317.

[5] Wünnemann K. et al. (2008), EPSL 269, 529-538.

[6] Wünnemann K. et al. (2006), *Icarus*, *180*, 514-527.

[7] Wünnemann K. et al. (2016), *M&PS*, *51*, 1762-1794.

[8] Melosh H. J. 2007. M&PS 42, 2079–2098.

[9] Pierazzo B. et al. (2005) GSA Special paper 384, 443–457.

EPSC Abstracts
Vol. 11, EPSC2017-286-1, 2017
European Planetary Science Congress 2017

The Orbit Planes of Impactors that Formed Elongated Martian Craters

E. Sefton-Nash (1), Z. Faes (1), O. Witasse (1) and B. Buchenburger (2).
(1) ESTEC, European Space Agency, The Netherlands, (2) KU Leuven, Belgium. (e.sefton-nash@cosmos.esa.int)

Abstract

Elongated craters can form from low angle impacts. The distinguishing morphological properties of elongated craters and their ejecta become more pronounced with decreasing impact angle, which allows ease of identification of craters formed by grazing impacts. Using remote sensing data and an ellipse-fitting algorithm, we update a pre-existing database of elongated craters on Mars [1, 2, 3] to better characterize selected properties regarding crater shape, location and estimated age. We use the retrieved impact direction to constrain the possible orbit planes that impactors may have originated from.

1. Database update

Our updated database comprises a GIS project registered to MOLA topography, THEMIS IR mosaics and relevant high-resolution visible images from HRSC, CTX and HiRISE. Shapefiles include preliminary estimates of crater geometric properties (centre position, size, eccentricity, azimuth, etc…).

2. Retrieving best-fit geometric parameters

To retrieve best-fit values of geometric parameters, we fit ellipses to crater rim crests (Fig. 1, upper). Idealized elongated crater rims are not necessarily ellipses, but this approach provides a numerically consistent way of retrieving crater geometry. We assess the goodness of fit, D, between crater rims and ellipses of given sizes and orientations. D is computed as the sum of the cartesian distance between all pairs of closest vertices in the model ellipse and the polygon that traces the crater rim crest. Provided that crater rims are sufficiently well-resolved, an unconstrained non-linear multivariate optimization (Nelder-Mead simplex direct search [4]) is then used to refine initial parameters (a_0,b_0,x_0,y_0,α_0) (Fig. 1, lower) to minimize D and retrieve the corresponding size and orientation parameters. To reduce influence on D of spatial distortion introduced by the map projection, distances are calculated in a local equirectangular projection with the point of true scale at the feature centroid.

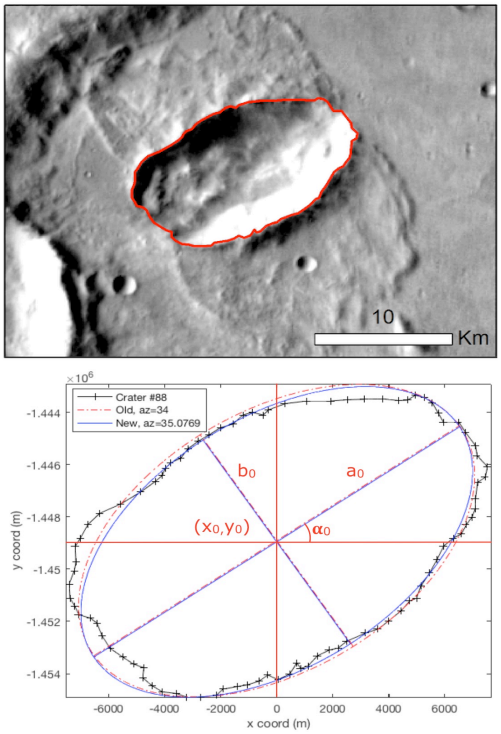

Figure 1: Upper – Example of mapped crater rim. Lower – Initial and best fit ellipse parameters for an elongated crater at 40.98°E, 24.46°S.

Oblique impacts form craters with morphology that can be used to ascribe the sense of the impact. For systematic assessment of features in our database, we identify several criteria whose cumulative indication of the same impact direction allow ascription of sense for the impactors trajectory. Asymmetric crater shapes could indicate that greater excavation energy was imparted to the surface at the point of first impact. The shape and distribution of ejecta is also

telling: In highly oblique cases, a butterfly pattern is present. In other cases ejecta distribution indicates greater deposition on one side, with a paucity forming a V-shaped zone of exclusion, opposite to the impact direction. Craters resulting from a body travelling in the prograde direction constitute ~50% of all craters in the database, while those in retrograde direction constitute ~35%. The remainder have undetermined impact directions.

3. Age

Impact chronology-derived ages from [5] show that most elongated craters on surfaces aged 3.7 to 4.1 Ga were formed by bodies travelling in a prograde direction. This presents an upper age limit for crater formation, but unit ages are consistent with the period in which Phobos and Deimos are hypothesized to have originated from a debris disk formed from a giant impact [6, 7].

4. Inclination of orbit planes

The inclination of the parent orbit plane for each elongated crater is calculated using the best-fit azimuth and crater latitude. The azimuth for a given elongated crater is interpreted to coincide with the ground-projection of the orbit from which it originated, represented as a great circle at an inclination, *i*. For a fixed rotation axis, the azimuth (measured counter-clockwise from East) and latitude of mapped craters is a function of only the orbit inclination. The relationship is independent of longitude and the position of the ascending node. We plot the azimuth, latitude and corresponding orbit inclination for selected features (Fig. 2 – upper). We exclude craters whose state of degradation or geomorphology warranted further investigation before azimuth and sense can be meaningfully retrieved, leaving 191 features from an initial 248.

5. Discussion

The distribution of orbit inclination with respect to Mars' present-day rotation axis indicates a relative paucity of impactors originating from low inclination orbits (Fig. 2 – lower). Thus, no low-angle impactors originated from Mars' present equatorial plane.

Moonlets in a debris disk with unstable, decaying orbits would impact Mars at a shallow angle [6, 7]. To investigate the decaying moonlet hypothesis, true polar wander of Mars' rotation axis [8, 9] is expected to be the predominant factor, because while obliquity cycles would indeed modify the relationship between latitude, azimuth and orbit plane inclination, a transient debris disk that lingered for several Ma would be expected to align with Mars' equator throughout obliquity variations. Further analysis will identify any groups of craters formed under the same orbit planes and rotation pole.

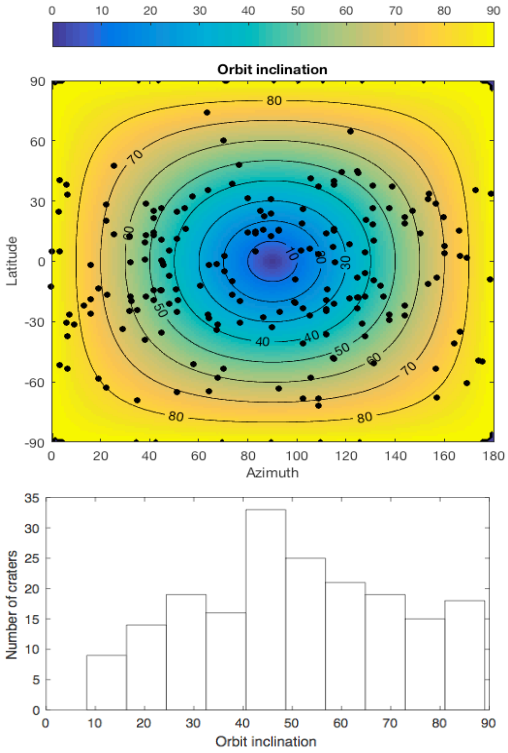

Figure 2: Upper – Distribution of best-fit elongated crater azimuths and latitude, and the retrieved orbit plane inclination, *i*, for Mars' current rotation axis. Lower – Distribution of *i* for 191 elongated craters.

References

[1] Schultz and Lutz-Garihan (1982) J. Geophys. Res. 87, (S01) p. A84–A96. **[2]** Bottke, W. F. et al (2000) *Icarus* 145, p. 108—121. **[3]** Buchenberger, B. (2011) *EPSC-DPS Joint Meeting 2011*, p. 738. **[4]** Lagarias, J. C. et al. (1998), *SIAM J. Optimization* 9 (1), p. 112-147. **[5]** Tanaka, K.L et al (2014) Geologic map of Mars: U.S. Geological Survey Scientific Investigations Map 3292. **[6]** Rosenblatt, P. et al (2016) *Nature Geoscience* 9, p. 581-583. **[7]** Craddock, R. A. (2011) *Icarus* 211(2), p. 1150-1161. **[8]** Schultz and Lutz (1988), *Icarus* 73, p. 91-141. **[9]** Bouley, S. et al. (2016), *Nature* 531, p. 344-347.

EPSC Abstracts
Vol. 11, EPSC2017-307, 2017
European Planetary Science Congress 2017

An age of both Ilumetsa structures – support of their impact origin

A. Losiak (1), J. Plado (2), A. Jõeleht (2), M. Szyszka (3), E.M. Wild (4), M. Bronikowska (3), C. Belcher (5), K. Kirsimäe (2), P. Steier (4).
(1) Planetary Geology Lab, Institute of Geological Sciences, Polish Academy of Sciences, Poland (anna.losiak@twarda.pan.pl); (2) Department of Geology, University of Tartu, Estonia (argo.joeleht@ut.ee, juri.plado@ut.ee, kalle.kirsimae@ut.ee), (3) Institute of Geology, Adam Mickiewicz University in Poznan, Poland (mateusz.szyszka@amu.edu.pl, malgorzata.bronikowska@amu.edu.pl); (4) VERA Laboratory, Faculty of Physics—Isotope Research & Nuclear Physics, University of Vienna, Austria (peter.steier@univie.ac.at, eva.maria.wild@univie.ac.at); (5) wildFIRE Lab, Hatherly Laboratories, University of Exeter, UK (c.belcher@exeter.ac.uk).

Abstract

Two Ilumetsa craters are listed as a proven meteorite impact site in the Earth Impact Database, but neither remnants of the projectile nor other identification criteria (e.g., PDFs) have been found up to this point [1]. Also, until now, the temporal relation between two Ilumetsa craters has not been established, as only larger structure was dated by determining ^{14}C age of gyttja (containing charcoal and silty sand) present within it [2]. In the present study we have established an age of both Ilumetsa craters by the ^{14}C dating of charcoal present within their ejecta blankets (similar method was used recently to date Kaali crater [3]). Both craters were formed between 7170 and 7000 cal. BP. Such temporal relation supports impact origin of those features.

1. Introduction

The Ilumetsa crater field in SE Estonia consists of two structures with diameters of 75-80 m (Ilumetsa Large - IL) and ~50 m (Ilumetsa Small - IS) with true depths of about 8 and 3.5 m, respectively [1, Fig. 1]. Both structures are surrounded with a rim up to a few meters high, which is highest in the eastern parts (max. rim heights are 4.5 and 1.5 m, respectively). The target rocks consist of Middle Devonian weakly cemented light-yellow to reddish silt- and sandstones, overlain by up to ~2.5 m thick layer of brown basal till and glaciofluvial sand. The rim consists of Devonian and Quaternary sands mixed with numerous till-like clayey sediment lenses. Deformed sedimentary beds and small thickness of glacial sediments favor an impact rather than a possible glacial (e.g., kettle- or sink-hole) origin of Ilumetsa.
Structures were previously dated by the ^{14}C analysis of gyttja and peat from the very bottom of IL [2]. The lowermost organic beds date back to 6030±100 14C years (7170-6660 cal. years BP; recalibrated with IntCal13). About 600 years older age (6542±50 14C years or 7570-7320 cal. years BC; IntCal13) of Ilumetsa was proposed by [4]. This date was based on peat with glassy spherules found in a depth of 5.7 m from the Meenikunno bog, ~6 km SWW from the structures. The spherules were reported as being up to a few millimeters in size and interpreted as dissipated melt or condensed vapor however their chemical composition (that could show relation to extraterrestrial material) was not reported.

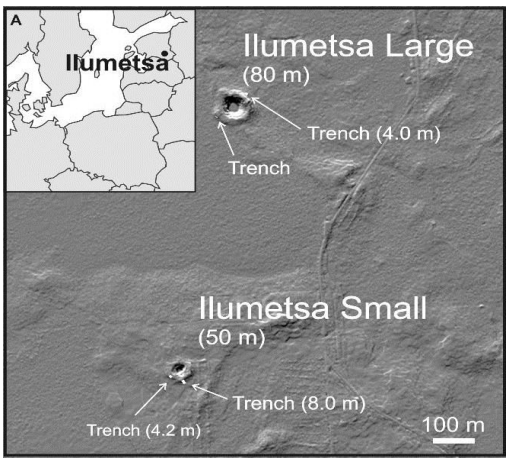

Figure 1. A) Location of the Ilumetsa craters. B) Digital elevation model of two Ilumetsa structures with location of the trenches (lengths of trenches are up to scale). A large flat area south from Ilumetsa Large is a bog.

2. Samples and methods

We have collected charcoal-containing samples from three trenches (two IS and one IL) located in the outer rim of both Ilumetsa structures, within their proximal ejecta blankets (Fig. 1). In *Ilumetsa Large* all charcoal samples came from a single 10-20 cm thick layer within the massive sand. This layer was slightly inclined outward the crater and located at the depth of 55-65 cm. Charcoal was unevenly distributed along the trench, being mostly present

at the distance between 1.7-2.8 m (measuring from the rim of the trench furthest away from the crater center). Most pieces of charcoal were very small, 1-2 mm in length, but few larger pieces (up to 1 cm) were identified. In the shorter trench of *Ilumetsa Small* only 6 charcoal samples were collected - but all of them were at least 5 mm in length (Ilume_S_2_3). All came from approximately the same depth, but did not form a continuous layer (smaller pieces than sampled were not found at this level). In the longer trench, significantly more charcoal was present, but its distribution within the strata was more complex. Similarly to the Kaali Main and IL crater, charcoal pieces were not distributed along the entire trench. In IL they were at the distance of 4.9-7 m (with a couple of pieces at 8 m distance – but on significantly lower depth than other pieces from the "main sequence"). Most of the charcoal was found within a lens-like (~20 cm in diameter) grey zone located at the depth of 65-85 cm. The color of this clayey-siltstone is most probably due to a large amount of charcoal and organic material. A large, 2.5 cm in length, piece of charcoal was found in the middle of this zone (Ilume_S_1_11g). A similar, but smaller grey zone was identified in one more place (50 cm from the first one). A couple of pieces were also found just above the level of ground water (90-110 cm). Some charcoal was also visible at the much shallower depths of 50 cm – below the soil level (Ilume_S_1_48). Most charcoal was dispersed as pieces of <5mm in length at a depth of 60-70 cm.

^{14}C dating was performed at the VERA (Vienna Environmental Research Accelerator) laboratory at the University of Vienna (Austria). The samples were chemically pretreated with the standard ABA (acid – base – acid) procedure used at VERA [5]).

3. Results and discussion

Ages determined for the charcoals from both craters are consistent with the previous ages obtained for the gyttja within the IL crater [2]. The most probable age of the craters is derived by combining youngest samples from both craters that are older than the gyttja within IL [2]. Those samples, even though they were taken from locations ~600 m from each other, are the same (95% probability). This approach helps to minimize an old wood problem in estimating age of those structures.

Old wood problem could explain slightly older ages of the samples from IL and IS (L_1_13, L_1_21, L_1_33, S_1_32, S_1_36). Three samples marked in a green box on Fig. 2 are ~1000 years older than the expected age of the craters. All of those samples come from grey circular zone with abundant large pieces of charcoal. We interpret them as remains of a pre-impact forest fire that was intermixed within ejecta. Two samples characterized by younger age were found on shallower depths (~50-60 cm) and probably post-date the impact and were introduced into subsurface by erosion of the crater rim.

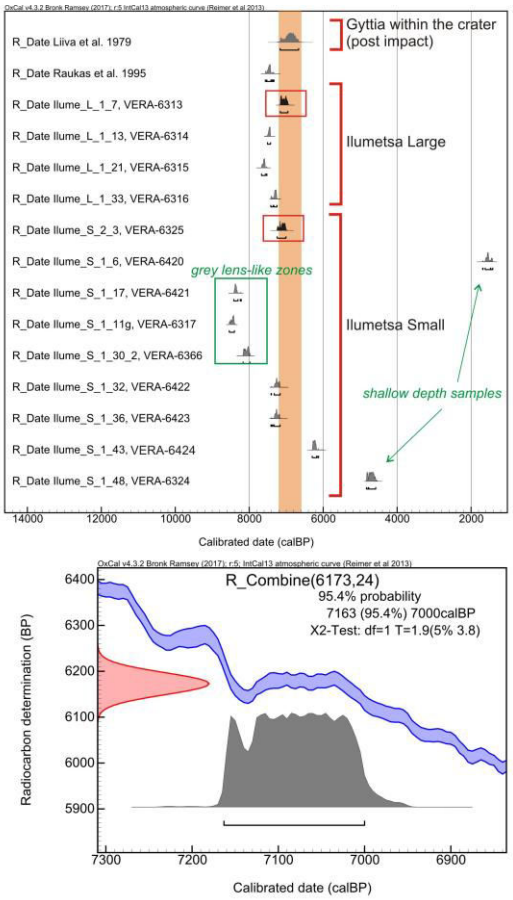

Figure 2: A) Detailed results of the ^{14}C dating of charcoal pieces found within both Ilumetsa craters. Vertical reddish stripe represents age of the sediments from inside the IL. B) Most probable age of the craters is derived from a combination of samples marked with red square on fig. 2A.

Acknowledgements

We are grateful to Barringer Family Fund for Meteorite Impact Research 2017, Estonian Research Council (project IUT20-34), National Science Centre (Poland) grant number UMO-2013/08/S/ST10/00586, and funds provided by the Institute of Geological Sciences Polish Academy of Sciences (project Kaali).

References

[1] Plado J., 2012. Meteorite impact craters and possibly impact-related structures in Estonia. MAPS 47: 1590-1605. [2] Liiva A., Kessel H. & Aaloe A., 1979. Age of the Ilumetsa craters. Eesti Loodus 12: 762-764. In Estonian. [3] Losiak et al. 2016 MAPS 51: 10.1111/maps.12616 [4] Raukas A., Tiirmaa R., Kaup E. & Kimmel K., 2001. The age of the Ilumetsa meteorite craters in southeast Estonia. MAPS 36: 1507-1514. [5] Wild et al. 2013. Radiocarbon 55: 599-607.

EPSC Abstracts
Vol. 11, EPSC2017-323-1, 2017
European Planetary Science Congress 2017

Does the gravity signature of lunar basins correlate with their ages?

D. Wahl (1) and J. Oberst (1,2)
(1) Technische Universität Berlin, Institute of Geodesy and Geoinformation Science, Strasse des 17. Juni 135, 10623 Berlin, Germany (daniel.wahl@tu-berlin.de, phone: +49 30 314 23331), (2) German Aerospace Center (DLR), Institute of Planetary Research, Rutherfordstrasse 2, 12489 Berlin, Germany

Abstract

The high-resolution gravity data provided by Gravity Recovery and Interior Laboratory (GRAIL) mission enables detailed modeling of subsurface structures of the Moon. We investigated the coherence between gravity signature of lunar impact basins and their relative ages. Since various factors seem to have major influence on the gravity signature no direct correlation to age could be found.

1. Introduction

Lunar impact basins provide insights into the early formation of terrestrial planets. By investigating their characteristics, we are able to learn more about the distribution, mass, and timing of the late accretion flux, as well as the state of the Moon during this time. The high-resolution gravity field, provided by the Gravity Recovery and Interior Laboratory (GRAIL) mission opens up new perspectives on the lunar impact basins and their formation. In combination with the topography obtained by the laser altimeter (LOLA) on board of the Lunar Reconnaissance Orbiter (LRO) mission, the characteristics of the basins described in former studies [1] may be revised. Utilizing the most recent data, we will set up a new inventory.

2. Is there a correlation between gravity signature and the age of lunar basins?

Based on studies by Neumann et al. [2] we investigated the correlation between the gravity signature of lunar basins and their relative ages. Bouguer gravity anomalies of lunar impact basins reveal a center peak, similar in size to the inner most topographic ring. Further out, a negative anomaly is found, which extends up to the rim crest (Fig. 1). The difference between the maximum gravity signal in the center and the lowest decrease towards the rim crest is defined as the Bouguer anomaly contrast. A correlation between this contrast and the size of an impact basin has been demonstrated [2].

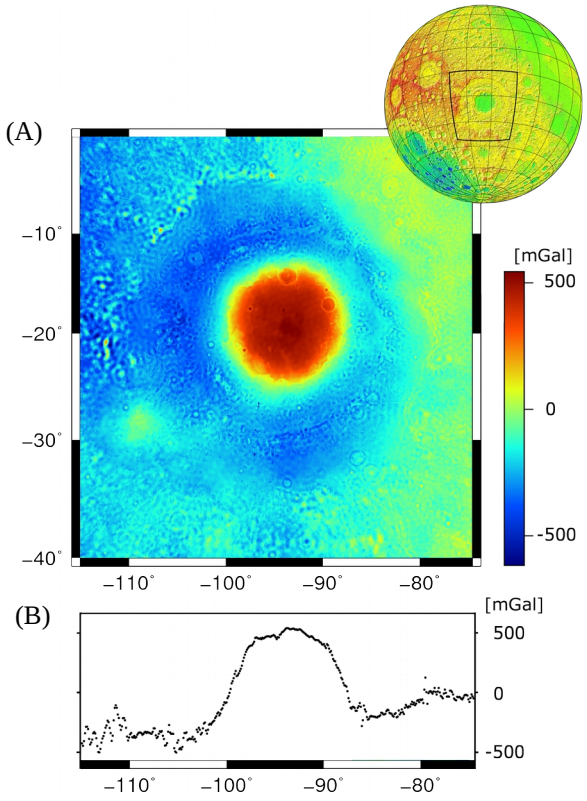

Figure 1: Orientale basin. (A) Top view of Bouguer gravity anomalies (B) Cross section of Bouguer gravity anomalies from west to east

We wish to test if the Bouguer anomaly contrast of impact basins correlates with their age: Since the

crust and the upper mantle of the Moon were much warmer in the past and thus less viscous, structures, formed during an impact, probably relaxed fast. For later events, when the interior was colder and therefore more viscous, these structures probably relaxed more slowly. We used the Bouguer anomaly contrast provided by Neumann et al. [2] and normalized them regarding the diameters of individual basins. Sorting the basins by the normalized contrast and comparing the order with basin ages determined from crater statistics [3] [4], no correlation could be found. In a next step, since the crustal thickness may have an influence on the thermal conditions and the speed of relaxation, we divide the basins in different groups, based on a crustal thickness map [5]. Also the separate groups did not show any correlation between gravity signature and the age of the impact basins.

3. Discussion and Outlook

We conclude that in addition to age, factors like a difference in thermal conditions or variations in thickness of mare fill must contribute to the gravity signature of lunar basins. Furthermore, the speed of relaxation is related to the basin dimension. The larger the diameter of an impact basin, the faster it relaxes [6]. All of these aspects proved the relaxation process to be more complex. Possible errors in estimated basin diameters, which were used for normalizing the Bouguer anomaly contrast, may also impact the outcome.

For a deeper understanding of the formation of lunar basins we will study basin candidates in more detail. We start our investigation with the working list of Wood [1]. Since the topography of lunar impact basins is often highly degraded due to subsequent cratering or erosion, especially older basins are difficult to recognize. The high-resolution gravity field offers new possibilities to identify lunar basins: besides the fact that subsurface structures mainly keep unaffected by processes occurring at the surface, during the basin formation mantle material was lifted up, causing a pattern of positive anomaly in the center, surrounded by a depression in gravity signature towards the rim crest (Fig. 1), where crustal material was removed [2]. This finding can be used for recognizing impact basins and defining their individual properties.

4. Conclusion

With the most recent data provided by GRAIL and LRO missions we are able to take a fresh look on lunar basins and their characteristics. High-resolution gravity data may help to identify basins and may give new constraints for impact simulations. No correlation is found between the gravity signatures of lunar basins and their relative ages.

Acknowledgments

This project is funded by the DFG SFB-TRR170. We wish to thank the scientists of the GRAIL and LRO missions for releasing their great products to the community.

References

[1] Wood, C. A.: unpublished data see: http://lpod.org/cwm/DataStuff/Lunar%20Basin.htm, accessed on February 06, 2017, 2004.

[2] Neumann, G. A. et al.: Lunar impact basins revealed by Gravity Recovery and Interior Laboratory measurements, Science Advances, Vol. 1, 9, pp. 1-10, 2015.

[3] Wilhelms, D. E.: The Geologic History of the Moon, U.S. Geological Survey Professional Paper, 1987.

[4] Fassett, C. I. et al.: Lunar impact basins: Stratigraphy, sequence and ages from superposed impact crater populations measured from Lunar Orbiter Laser Altimeter (LOLA) data, J. Geophys. Res. Planets, Vol. 117, pp. 1-13, 2012.

[5] Miljcovic, K. et al.: Subsurface morphology and scaling of lunar impact basins, J. Geophys. Res. Planets, Vol. 121, 9, pp. 1695-1712, 2016.

[6] Turcotte, D. L. and Schubert, G.: Geodynamics, Cambridge University Press, 2014.

EPSC Abstracts
Vol. 11, EPSC2017-357, 2017
European Planetary Science Congress 2017

On the relative importance of thermal and chemical buoyancy in impact-induced melting on Mars

T. Ruedas (1,2), D. Breuer (2)
(1) Institute for Planetology, University of Münster, Germany, (2) Institute of Planetary Research, German Aerospace Center (DLR), Berlin, Germany (t.ruedas@uni-muenster.de)

Abstract

We ran series of 2D numerical mantle convection simulations of the thermochemical evolution of a Mars-like planet. In order to study the importance of compositional buoyancy of melting mantle, the models were set up in pairs of one including all thermal and compositional contributions to buoyancy (TC) and one accounting only for the thermal contributions (T). Single large impacts were introduced as causes of additional strong local anomalies, and their evolution in the framework of the convecting mantle was tracked. They confirm that the additional buoyancy provided by the depletion of melting mantle can establish a global stable stratification of the convecting mantle and throttle crust production. Furthermore, it is essential in the stabilization and preservation of local compositional anomalies directly beneath the lithosphere and offers a possible explanation for the existence of distinct, long-lived reservoirs in the martian mantle. Such anomalies will be detected by gravimetry rather than by seismic or heat flow measurements. The crustal thickness can be locally overestimated by up to 15–22 km if impact-induced density anomalies in the mantle are neglected.

1. Introduction

Convection in planetary mantles is driven by buoyancy that results from density variations, which may have thermal or compositional causes. We study the relative importance of the thermal and compositional contributions to the buoyancy of melt-induced density heterogeneities in Mars by coupling two-dimensional, fully dynamical convection models with a detailed model of the mineralogy and material properties of martian peridotite (e.g., [1, 2]). The main focus lies on the anomalies created by giant impacts, which lead to particularly intense, high-degree melting that may reach deeper than the regular global asthenospheric melting zone. We investigate the differences in the evolutions of models with only thermal and with both thermal and compositional buoyancy for impacts of different sizes; the compositional aspect has been neglected in most previous studies (e.g., [3, 4, 5]).

2. Method

The convection code is a modified version of STAGYY [6] and solves the conservation equations of mass, momentum, and energy in the compressible, anelastic approximation on a two-dimensional spherical annulus grid [7]. Material properties are derived from mineral physics improved and updated after [1]. For the models with purely thermal buoyancy, the compositional contribution was suppressed by forcing the density (and other physical properties) to remain at the value they would have for undepleted mantle, although the melting degree and changes in trace element composition are changed as usual.

The impact itself is represented as an instantaneous thermal anomaly, with shock-heating derived from the peak shock pressure based on the impedance-match model (cf. [4]); the material properties of the target are derived from the convection model, and the pressure decay with distance from the impact center is given by the "inverse-r" parameterization from [8]. As we model the impacts after existing martian craters, we use their observed final diameters D_f as input and deduce impact parameters such as the impactor size from them using empirical scaling laws [9].

3. Model

The general model parameters used in all models are listed in Table 1. Impacts of three different sizes corresponding to the Huygens ($D_\mathrm{f} = 467.25\,\mathrm{km}$), Isidis ($D_\mathrm{f} = 1352\,\mathrm{km}$), and Utopia ($D_\mathrm{f} = 3380\,\mathrm{km}$) impact basins, respectively, are considered. All impacts are assumed to occur at 4 Ga, i.e., 400 My after the model run begins; this choice approximates reasonably well the estimated age of the three craters and ensures that the model has developed a lithosphere of

a certain thickness, comparable to that of Mars at that age. Most models assumed a bulk water content of 36 ppm by mass, as proposed by [10], but we also ran some models with the higher initial concentrations; this parameter affects mostly the rheological behavior.

Table 1: Important model parameters

Mantle thickness	1659.5 km
Surface temperature	215 K
Init. potential temperature	1700 K
Init. core superheating	150 K
Simple/complex transition	5.6 km
Bulk silicate Mars Mg#	0.75
Present K, Th, U	305 ppm, 56, 16 ppb
Init. bulk water content	*36*, 144 ppm

4. Results

Figure 1 shows the temperature and melting degree fields for the model pair with an Isidis-sized impact and a planet with an initial bulk water content of 36 ppm. In the model with both thermal and compositional buoyancy (TC), the strongly depleted compositional anomaly from the impact, visible as a dark red patch at 400 My, spreads beneath the lithosphere and remains there as a stable layer, which is progressively incorporated into the growing thermal lithosphere. By contrast, the compositional anomaly in the purely thermal model (T) is mixed back into the mantle and leaves no coherent trace that survives to the present. The thermal anomaly decays by diffusion within a few tens of millions of years in both cases. The additional melt production results in additional crust production at the impact site, but the net effect is not necessarily a thickened crust, because the impact itself also removes a large amount of crustal material, and a part of it is deposited outside the final crater as ejecta. The results further suggest that the crustal thickness can be locally overestimated by up to 15–22 km if impact-induced density anomalies in the mantle are neglected.

The different behavior displayed by the two model variants is due to the additional density deficit caused by compositional changes of the melting rock, especially the loss of iron. The density deficit suggests that the signature of an impact-generated compositional anomaly may be detectable by gravimetric methods, but a detection with seismic means would not be expected with instrumentation whose deployment on Mars can be expected within the next decades.

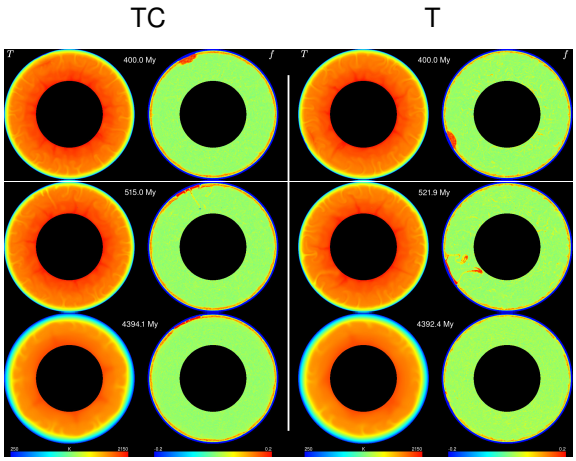

Figure 1: Temperature (T) and composition (f, positive values indicate depletion/melting degree) fields for the models with an Isidis-like impact.

Acknowledgements

TR was supported by grant Ru 1839/1-1 from the Deutsche Forschungsgemeinschaft (DFG). The numerical calculations were carried out on the computational resource ForHLR II at the Steinbuch Centre for Computing, Karlsruhe Institute of Technology, funded by the Ministry of Science, Research and the Arts Baden-Württemberg and DFG.

References

[1] T. Ruedas, et al. (2013) *PEPI* 216:32.

[2] T. Ruedas, et al. (2017) *JGR Planets* submitted.

[3] C. C. Reese, et al. (2002) *JGR* 107(E10):5082.

[4] W. A. Watters, et al. (2009) *JGR* 114:E02001.

[5] J. H. Roberts, et al. (2012) *Icarus* 218(1):278.

[6] P. J. Tackley (2008) *PEPI* 171(1–4):7.

[7] J. W. Hernlund, et al. (2008) *PEPI* 171(1–4):48.

[8] T. Ruedas (2017) *Icarus* 289:22.

[9] H. J. Melosh (1989) *Impact cratering: a geologic process*, Oxford University Press.

[10] H. Wänke, et al. (1994) *Phil Trans R Soc Lond* A 349:285.

[11] C. M. Bertka, et al. (1998) *EPSL* 157:79.

EPSC Abstracts
Vol. 11, EPSC2017-361, 2017
European Planetary Science Congress 2017

Interior responses to impacts by different impactor types

T. Ruedas (1,2), D. Breuer (2)
(1) Institute for Planetology, University of Münster, Germany, (2) Institute of Planetary Research, German Aerospace Center (DLR), Berlin, Germany (t.ruedas@uni-muenster.de)

Abstract

We use scaling laws for impacts to estimate the differences in the effects on the interior of a planet that impactors with different parameters and properties have even if they produce impact craters with the same diameter at the surface. The long-term effects of such "isocrater" impacts on planetary evolution are then also studied with numerical models of mantle convection for different bodies, but especially for Mars. The results support the notion that the vast majority of large impacts was caused by asteroids rather than other bodies such as large comets.

1. Introduction

A number of numerical mantle convection studies from the past two decades have investigated the effects of very large meteorite impacts on mantle dynamics in terrestrial planets, especially Mars (e.g., [1, 2]). On the grounds that most observed craters seem to have been produced by collisionally evolved bodies, probably main-belt asteroids (e.g., [3, 4], the impactors were generally assumed to be rocky and have material parameters similar to those of the target. However, the statistical analysis does not imply that all craters derive from an S-type asteroid, as there is a significant fraction of impactors whose properties differ substantially from those of the target, and the dynamical effects in the interior may be quite different even if the final crater is similar; candidate alternative impactors include C-type asteroids and comets. It is generally not possible to deduce the nature of the impactor from the final crater, because the remnants of the impactor are rarely preserved.

2. Theory

The final crater results from the collapse of the transient crater, and their diameters D_f and D_tr are related by empirical scaling relations. The relation between D_tr and the characteristics of the impactor is derived by dimensional analysis. Combining both yields

$$D_\mathrm{f} = 1.3836 \left(\frac{\varrho_\mathrm{imp}}{\varrho}\right)^{0.377} \frac{D_\mathrm{imp}^{0.88}}{D_\mathrm{s2c}^{0.13}} \frac{v_\mathrm{imp}^{0.497}}{g^{0.249}} \quad (1)$$

for complex craters, where D_imp is the diameter of the impactor, ϱ and ϱ_imp the densities of the target and the impactor, v_imp is the velocity of the impactor (or rather its vertical component), D_s2c is the simple-to-complex transition diameter, and g is gravity (e.g., [5]); the numerical values of the coefficient and exponents vary with certain target properties and are chosen here to correspond to a frictionless, pore-free material. In this equation, ϱ_imp and v_imp are not known for a given crater and may vary widely between different impactor types. Hence the condition for two impactors 1 and 2 to produce a final crater of the same diameter on the same target is given by $D_\mathrm{f1} = D_\mathrm{f2}$:

$$\frac{D_\mathrm{imp1}}{D_\mathrm{imp2}} = \left(\frac{\varrho_\mathrm{imp1}}{\varrho_\mathrm{imp2}}\right)^{-0.43} \left(\frac{v_\mathrm{imp1}}{v_\mathrm{imp2}}\right)^{-0.56} = \delta_{12}, \quad (2)$$

for both simple and complex craters; this defines a set of isocrater impacts. Figure 1 shows the ratio of impactor diameters, δ_{12}, for isocrater impacts, whereby impactor 2 is chosen as a common reference impactor, namely an S-type asteroid. The isolines thus show how strongly the size of impactor 1 must differ from that reference in order to produce a crater of the same size, for any combination of density and velocity, which are also normalized to the reference.

For the dynamics of the interior, it is the subsurface features of an impact rather than the crater that are of primary interest, but their geometry and properties are more difficult to study and less well described in terms of an analytical model. In the literature (e.g., [6]), the depth of penetration is often found to be proportional to the square or cube root of the density ratio $\varrho_\mathrm{imp}/\varrho$, and the impact velocity is taken to a power between 1/3 and 2/3. We combine the square-root relation for the density with the widely used formula by [7] for the depth to the center of the isobaric core of the shocked volume into the relation

$z_{\rm ic} = a_z D_{\rm imp} v_{\rm imp}^{b_z} \sqrt{\varrho_{\rm imp}/\varrho}$; future numerical impact simulations should test whether empirical fits yield an exponent of the density ratio that is significantly different from 0.5. The ratio of the depths of the isobaric cores for two isocrater impacts then follows by combination with eq. 2:

$$\frac{z_{\rm ic1}}{z_{\rm ic2}} = \left(\frac{\varrho_{\rm imp1}}{\varrho_{\rm imp2}}\right)^{0.07} \left(\frac{v_{\rm imp1}}{v_{\rm imp2}}\right)^{b_z-0.56} = \zeta_{12}; \quad (3)$$

we use the value $b_z = 0.361$ from [7].

The other principal geometrical characteristic of an impact is the size of the shocked volume, which is often measured in terms of the size of the isobaric core, where the shock pressure shows relatively little variation. We choose it to be the position of the inflexion point of the shock pressure decay curve defined by the "inverse-r" approximation for shock pressure decay [8], and applying again the isocrater criterion eq. 2, the ratio of the isobaric cores of two isocrater impacts is

$$\frac{r_{\rm infl1}}{r_{\rm infl2}} = \delta_{12} \left(\frac{n_1 - 1}{n_1 + 1} b_1\right)^{\frac{1}{n_1}} \Bigg/ \left(\frac{n_2 - 1}{n_2 + 1} b_2\right)^{\frac{1}{n_2}} . \quad (4)$$

The velocity dependences are complicated, because the parameters b and n are material-dependent functions of $v_{\rm imp}$ as well, and so the ratios become dependent on the target planet as well as on the impact angle.

Apart from the geometrical relations, there are also semi-empirical relations between impactor parameters and the amount of melt produced in an impact to which similar considerations can be applied.

Figure 1 applies to impacts of impactors that differ in density, velocity, and size but result in a crater of the same final diameter. The isolines show how much larger or smaller, relative to an S-type asteroid, an impactor of some chosen density and velocity has to be in order to produce the same crater. The center of the isobaric core would be shallower for all alternative impactor types, but the melt volume produced by alternative impactors would be larger by up to 40%.

3. Model

We also carried out numerical mantle convection simulations with a modified version of STAGYY [9, 10] in which the impact is represented as an instantaneous thermal anomaly. The models show that the effects on the interior of isocrater impacts by impactors of different types can vary considerably, especially between rocky impactors with low to intermediate velocities and fast, ice-rich impactors.

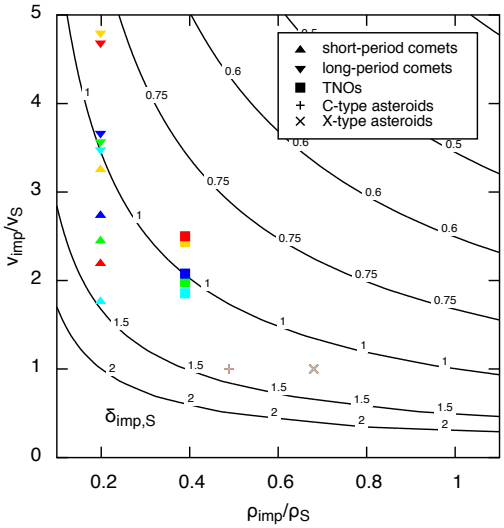

Figure 1: Ratio of impactor diameters for isocrater impacts as functions of the ratios of densities and impactor velocities (eq. 2). The symbols mark averages pertaining to the target (cyan: Mercury, green: Venus, blue: Earth, gold: Moon, red: Mars, grey: all targets).

Acknowledgements

TR was supported by grant Ru 1839/1-1 from the Deutsche Forschungsgemeinschaft (DFG) and SFB-TRR 170. The numerical calculations were carried out on the ForHLR II supercomputer at the Steinbuch Centre for Computing, Karlsruhe Institute of Technology, funded by the state of Baden-Württemberg and DFG.

References

[1] W. A. Watters, et al. (2009) *JGR* 114:E02001.

[2] J. H. Roberts, et al. (2012) *Icarus* 218(1):278.

[3] B. A. Ivanov, et al. (2002) in *Asteroids III* 89–101 University of Arizona Press, Tucson, Arizona.

[4] R. G. Strom, et al. (2005) *Science* 309(5742):1847.

[5] S. C. Werner, et al. (2015) in *Treatise on Geophysics* (2nd edn.), vol. 10, Elsevier.

[6] J. K. Dienes, et al. (1970) in *High-Velocity Impact Phenomena* chap. 3, Academic Press.

[7] E. Pierazzo, et al. (1997) *Icarus* 127(2):408.

[8] T. Ruedas (2017) *Icarus* 289:22.

[9] P. J. Tackley (2008) *PEPI* 171(1–4):7.

[10] T. Ruedas, et al. (2013) *PEPI* 216:32.

EPSC Abstracts
Vol. 11, EPSC2017-500, 2017
European Planetary Science Congress 2017

Raman spectroscopy on experimentally shocked plagioclase and applications to the Martian regolith breccia NWA8171

M. C. Langenhorst (1), V. Iancu (1), N. Tarcea (1), F. Langenhorst (2) and J. Popp (1)
(1) Institut für Physikalische Chemie, Friedrich-Schiller-Universität Jena, Helmholtzweg 4, 07743 Jena, Germany, (2) Institut für Geowissenschaften, Friedrich-Schiller-Universität Jena, Carl-Zeiss-Promenade 10, 07745 Jena, Germany

Abstract

We present here Raman spectra of experimentally shocked plagioclase in order to calibrate the spectral changes as a function of shock pressure. The effects of shock compression are distinct band shift and broadening as well as appearance of new broad bands. The application of these data to a Martian meteorite show that it has experienced only weak shock metamorphism (< 5 GPa).

1. Introduction

Raman spectroscopy is extensively developed for remote and surface exploration missions to planetary bodies in our solar system [1]. It is regarded as a powerful technique to determine the mineralogical and chemical compositions of regoliths on these bodies. The minerals in regoliths and their structural states are however often modified by strong impact events. It is hence important to calibrate the spectroscopic changes of typical surface minerals as a function of shock pressure by aid of shock experiments. The applicability of the experimental Raman data can finally be tested on meteorites.

In this study we have used Raman spectroscopy to analyse the structural changes of experimentally shocked plagioclase (oligoclase). Optical, X-ray diffraction, Infrared (IR) spectroscopy and Electron Paramagnetic Resonance (EPR) data of some of our samples were previously reported by [2,3]. The Raman data were applied to NWA8171, the only known regolith breccia among the Martian meteorites [4].

2. Experiments and samples

High-explosive (TNT, Comp. B) shock experiments were carried out at the Ernst-Mach-Institut (Freiburg, Germany) on oligoclase from Lake Muskwa, Canada, with the composition $Ab_{78}An_{20}Or_2$ [2]. According to graphical impedance matching techniques, the pressures achieved were 26, 30, 34, 37.5, and 52.5 GPa.

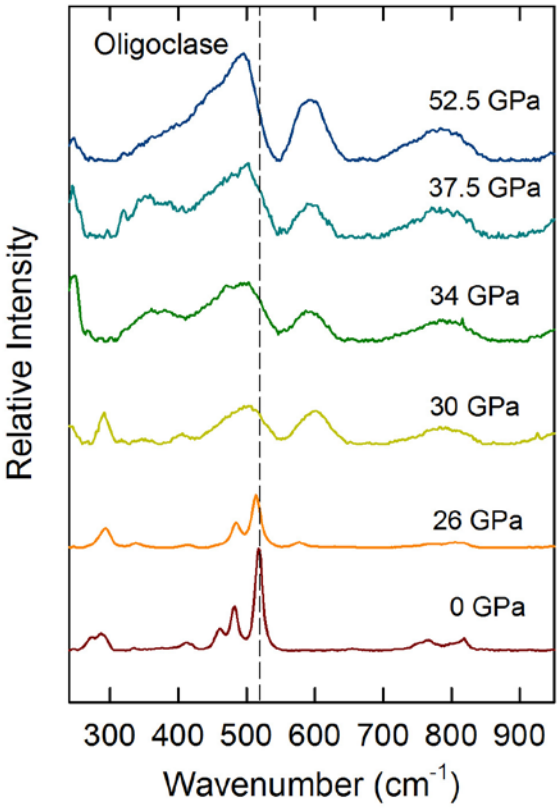

Figure 1: Raman spectra of unshocked and experimentally shocked oligoclase.

Raman spectroscopic measurements were performed using a RamanRXN1 device from Kayser Optical Systems Inc. equipped with a 785 nm laser. Other excitation wavelengths (514 nm, 532 nm and 1064 nm) were tested, as well. Strong fluorescence occurred in all measurements, especially in the

spectra of highly shocked oligoclase. Measurements with the 785nm laser turned out to yield the best quality for the given set of samples.

The changes observed in spectral features were used to infer the shock conditions in the Martian meteorite NWA8171, a polymict regolith breccia with a basaltic bulk composition. The most abundant phase in this meteorite is plagioclase (andesine).

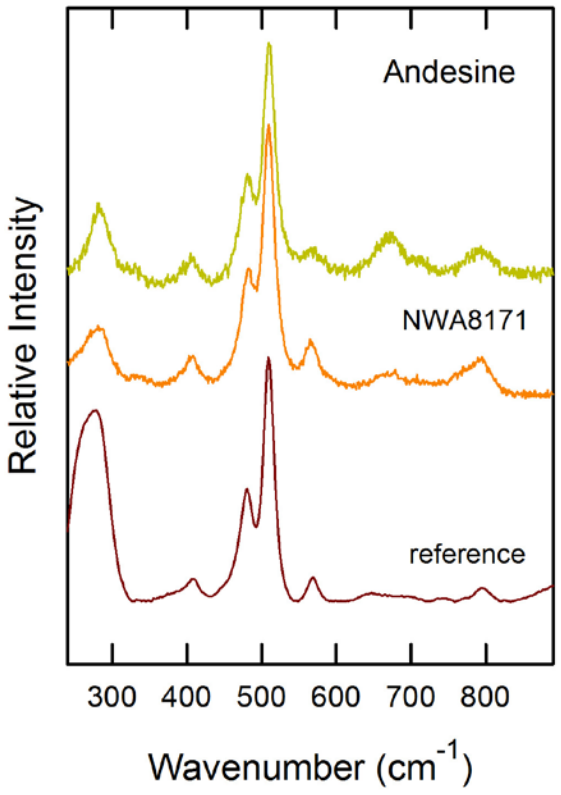

Figure 2: Comparison of Raman spectra of reference andesine with those of andesine in NWA8171.

3. Results and discussion

Fig. 1 shows a compilation of Raman spectra of unshocked and shocked oligoclase samples. The unshocked crystalline oligoclase shows several well-defined Raman active vibrational modes:

Lattice and deformation modes between 100 and 350 cm^{-1}, symmetric T–O stretching modes and O–T–O deformation modes in TO_4 groups between 400 and 550 cm^{-1}, and asymmetric T–O stretching modes and O–T–O deformation modes in TO_4 groups at even higher wavenumber [5].

The Raman spectra of shocked oligoclase display much broader bands and an increase of the fluorescence background. The strongest Raman band is at 517 cm^{-1} for the unshocked sample. It systematically broadens and shifts to lower wavenumbers as a function of increasing pressure. The band is centred at 513, 506, 497, and 495 cm^{-1} for pressures of 26, 30, 34 and 52.5 GPa, respectively.

We also note the appearance and intensity increase of two broad bands in spectral range of the asymmetric modes at about 600 and 790 cm^{-1}. These observations point to a progressive distortion and amorphization of the plagioclase structure.

The Raman spectra of reference andesine and oligoclase are overall very similar (Figs. 1 and 2); there are only subtle spectral differences due to the different compositions of both plagioclases. The main band in the reference andesine spectrum is at 509 cm^{-1}. The Raman bands of andesine from NWA8171 are only slightly broader and are not shifted with respect to the reference spectrum. Therefore we conclude that the plagioclase in the Martian regolith breccia has only experienced weak shock metamorphism (< 5 GPa). This conclusion is in line with optical observations that reveal undulatory extinction only in few grains.

Further Raman measurements are in progress to extend the database to a larger variety of plagioclases and to test the applicability of band shifts and broadening as pressure calibrants.

Acknowledgements

V.I., N.T., F.L. and J.P. acknowledge ‘Deutsches Zentrum für Luft- und Raumfahrt (DLR)’ for the financial support (grant nr. 50QX1301). F.L. thanks the Deutsche Forschungsgemeinschaft for funds provided by the Leibniz programme (LA 830/14-1).

References

[1] Wang A. et al. (2015) *Planetary and Space Sciences, 112*, 23-34.
[2] Ostertag R. (1983) *JGR, 88*, B364-B376.
[3] Langenhorst F. (1989) *Meteoritics, 24*, 291.
[4] Agee A.B. et al. (2013) *Science, 339*, 780-785.
[5] Freeman J. J. et al. (2008) *Canadian Mineralogist, 46*, 1477-1500.

EPSC Abstracts
Vol. 11, EPSC2017-522, 2017
European Planetary Science Congress 2017

Using large impacts to constrain the thermal evolution of the terrestrial planets

S. Padovan (1), N. Tosi (1,2), A.-C. Plesa (1), and T. Ruedas (1,3)
(1) DLR—German Aerospace Center, Berlin, Germany; (2), Technische Universität, Berlin, Germany; (3) University of Munster, Germany (sebastiano.padovan@dlr.de)

Abstract

The surfaces of Mercury, the Moon, and Mars are largely the results of interior processes that operated over the age of the solar system. These surfaces are also the location of copious amount of data (e.g., imaging, spectrometry). However, the only direct constraints available when investigating the interior evolution of terrestrial planets are related to the nature (volcanic/primordial), volume, and age of the crust. In this work we compute thermal evolution models for Mercury, the Moon, and Mars constrained by the properties of their crusts. We evaluate the geodynamical effects of large impacts in the interior evolution of each body. We focus on reproducing the inferred volume and time of emplacement of the volcanic infillings associated with large impact basins. This approach combines local datasets with global thermal histories of the terrestrial planets. We validate this method on Mercury by showing that we can reproduce the physical and spectral properties of its large basins. We apply the same methodology to Mars and the Moon.

1. Introduction

The crusts of Mercury and Mars are mostly volcanic, the result of partial melting associated with mantle convection [1,2]. The primordial lunar crust is only partially covered by volcanic material in the relatively large mare provinces, located mostly in the nearside hemisphere and in association with large impact basins [3]. Thermal or thermo-chemical evolution models are broadly consistent with the observed properties of the crusts of Mercury, Mars, and the Moon [e.g., 4—6].

The possible causal link between large impacts and subsequent impact-induced volcanism has been explored both for the Moon [e.g., 7] and for Mercury [8]. However, none of the previous works explicitly took advantage of the local datasets related to large impact basins.

2. Methods

We use the code GAIA [9] to compute thermal evolution histories for Mercury, Mars, and the Moon. We compute crustal production resulting from partial melting in the mantle. We take into account extraction of the incompatible heat sources and the modification of the solidus as a result of partial melting in the mantle. We vary the mantle reference viscosity, the amount of radiogenic material in the mantle, and the thickness of a low-conductivity regolith layer. The effect of large impacts is computed with scaling laws [e.g., 8]. We focus on the volume, depth of the source region, and temporal extent of melting associated both with mantle convection and with the effects of large impacts.

3. Constraints on the evolution

The volume of the volcanic crusts of Mercury and Mars [10,11] and the volume of basaltic volcanism on the Moon [e.g., 5] provide an estimate of the cumulative amount of partial melting produced in the mantles of these bodies. The timing of the major volcanic eruptions [2,12] provides an indication of the evolution of the thermal state of the mantle. The end of major volcanic eruptions would indicate the ending of major production of partial melt in the mantle. Large impact basins are often observed to contain volcanic material in their interiors [e.g., 13]. Stratigraphic analyses and crater counting can provide estimates for the volume and time of emplacement of this volcanic material [e.g., 14].

4. Results

Figure 1 shows crustal production from partial melting associated with mantle convection as a function of time obtained for representative thermal evolution models of Mercury and Mars. The curves are compatible both with the inferred volume of the crusts of these bodies [10,11] and with the timing of volcanic activity recorded on their surfaces [2,12].

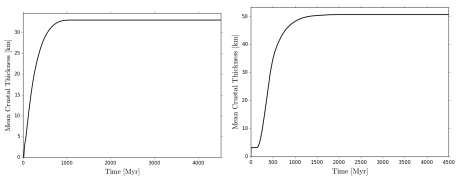

Figure 1: Crustal thickness evolution for Mercury (left) and Mars (right) from 2D cylindrical simulations of mantle convection. The thicknesses at 4.5 Gyr are compatible with the values inferred from the analysis of gravity and topography data [10,11].

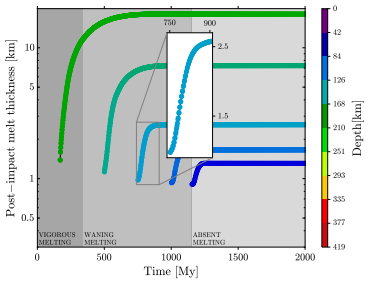

Figure 2: Melt production following an impact forming a Caloris-sized basin on Mercury at different epochs. Thickness values refer to melt produced below the final basin. Colors indicate the source depth of the melt. The grey background indicates the amount of melting associated with mantle convection (from Figure 1).

Given the large number of parameters that are required in thermal evolution models, these two constraints are relatively easy to satisfy. For an impact forming a Caloris-size basin on Mercury at different epochs in the evolution of the planet, Figure 2 shows the predicted amount of in-basin volcanism and depth of the source region. The event highlighted in the box corresponds to the time of the Caloris forming impact event on Mercury. The predicted volume and time of emplacement match the corresponding values inferred from stratigraphy and crater counting in the Caloris basin [13, 14]. These quantities depend on the values of the parameters of the evolution model, thus illustrating the possibility of including local constraints in a global evolution code approach. Further comparisons with physical and spectral properties of large basins on Mercury validate the method [15].

5. Conclusions

We present a novel method that takes advantage of both global and local constraints in computing thermal evolution models for Mercury, Mars, and the Moon. We test the method on Mercury, showing that it can properly reproduce the observed physical and spectral properties of the large basins observed on the surface. Results regarding the application of the method to Mars and the Moon will be presented.

References

[1] Denevi, B. W., et al., J. Geophys. Res. Planets, 118, pp. 1—17, 2013.

[2] Ehlmann, B. L., et al., Nature, 479, pp. 53—60, 2011.

[3] Wieczorek, M. A., et al., Rev. Mineral. Geochem., 60, pp. 221—364, 2006.

[4] Tosi, N., et al., J. Geophys. Res. Planets, 118, pp. 2474—2487, 2013.

[5] Laneuville, M., et al., J. Geophys. Res., 118, pp. 1435—1452, 2013.

[6] Plesa A.-C. et al., J. Geophys. Res. Planets, 120, pp. 995—110, 2015.

[7] Elkins-Tanton, L. T., et al., Earth Planet. Sci. Lett., 222, pp. 17—27, 2004.

[8] Roberts J. H. and Barnouin O. S.:, J. Geophys. Res. Planets, 117, pp. 1—15, 2012.

[9] Hüttig, C., et al., Phys. Earth Planet. Inter., 220, pp. 11—18, 2013.

[10] Padovan, S., et al., Geophys. Res. Lett., 42, pp. 1029—1038, 2015.

[11] Wieczorek, M. A. and Zuber, M. T., J. Geophys. Res., 109, pp. 1—16, 2004.

[12] Byrne, P. K., et al., Geophys. Res. Lett., 43, pp. 1—9, 2016.

[13] Fassett, C. I., et al., J. Geophys. Res., 117, pp. 1—15, 2012.

[14] Ernst, C. M., et al., Icarus, 250, pp. 413—429, 2015.

[15] Padovan, S., et al., LPSC XLVIII, abstract 1809, 2017.

EPSC Abstracts
Vol. 11, EPSC2017-561, 2017
European Planetary Science Congress 2017

The impact of meteoritic impacts on the early Martian environment

M. Turbet (1), F. Forget (1), V. Svetsov (2), H. Tran (1), O. Karatekin (3), O. Popova (2) and C. Gillmann (3)

(1) Laboratoire de Météorologie Dynamique, Sorbonne Universités, UPMC Univ Paris 06, CNRS, 4 place Jussieu, 75005 Paris, France (martin.turbet@lmd.jussieu.fr); (2) Institute for Dynamics of Geospheres, Russian Academy of Sciences, Leninskiy Prospekt 38-1, Moscow 119334, Russia; (3) Royal Observatory of Belgium, Avenue Circulaire 3, 1180 Uccle, Belgium.

1. Introduction

There is now a large number of evidences that liquid water flowed on early Mars: high erosion rates, sedimentary deposits, hydrated minerals and geomorphological clues including dry river beds and lakes [1-14]. Sophisticated climate modelling under ancient Mars conditions assuming a faint young Sun and CO_2-dominated atmospheres have not been able yet to produce liquid water or significant precipitations anywhere on the planet [15,16], unless incorporating additional reduced greenhouse gases, e.g. CH_4 and/or H_2 [17-19].

It has been suggested that warm & wet conditions required to explain the formation of the aforementioned geological evidences could have been transient and produced in response to meteoritic impacts [16,20-23]. This scenario is seducing because the formation of the valley networks is contemporaneous with the Late Heavy Bombardment that took place 3.8 billions years ago.

We model here the environmental effect of meteoritic impacts to explore if they could trigger the warm conditions and the precipitation rates required to explain the formation of the valley networks.

2. Method

This study was performed with the 3D LMD Generic Global Climate Model (GCM). The model works with a sophisticated water cycle that includes the formation of H_2O and CO_2 ice clouds [15,16,24], and for various atmospheres made of $CO_2/N_2/H_2O$. Simulations were performed with resolution grids of 3°x3°x40 levels (in latitude x longitude x altitude). We used both the present-day MOLA and ancient Mars topographies [24-26], when appropriate. More details on the model can be found in [15,16,24,26,27].

3. Results

3.1 Large impact events

We simulated the climatic impact of large meteoritic impactors ($D_{impactor}$>100km, N_{events} ~ 10) hitting the surface of Mars at velocities ~10km/s, by forcing initially the atmosphere/surface/subsurface at temperatures up to 600 Kelvins, and vaporizing up to several bars of water vapor.

Our main result is that, *whatever the initial impact-induced temperatures and water vapor content injected, warm climates cannot be stable and are in fact short-lived* (lifetime of ~ 5-7 martian years per bar of water vapor injected). The results of Segura et al. 2012 [22], which would require extremely high supersaturation levels of water vapor to work, are at odd with our findings. Note that we obtain minimum outgoing thermal radiation fluxes that are in good agreement with recent studies on the runaway greenhouse [28].

When a hot, steam atmosphere forms after a large meteoritic impactor hits early Mars, our 3D GCM simulations indicate that the IR thermal emission to space is roughly 200W/m² higher than the incoming stellar radiation (under Faint Young Sun), *everywhere on the planet*. At the altitude of IR emission to space, water vapor condenses, releasing ~ 200W/m² of latent heat, everywhere on the planet. Consequently, a 100%, thick cloud cover forms, producing precipitation (rainfall, here) uniformly distributed on the planet. This mechanism is summarized in Fig 1.

Warm & wet conditions that follow the largest impact events recorded on Mars should not only have been short-lived, but should also have produced thick 100% cloud coverage, responsible for precipitation patterns uniformly distributed on the planet, and thus uncorrelated with the position of the valley networks.

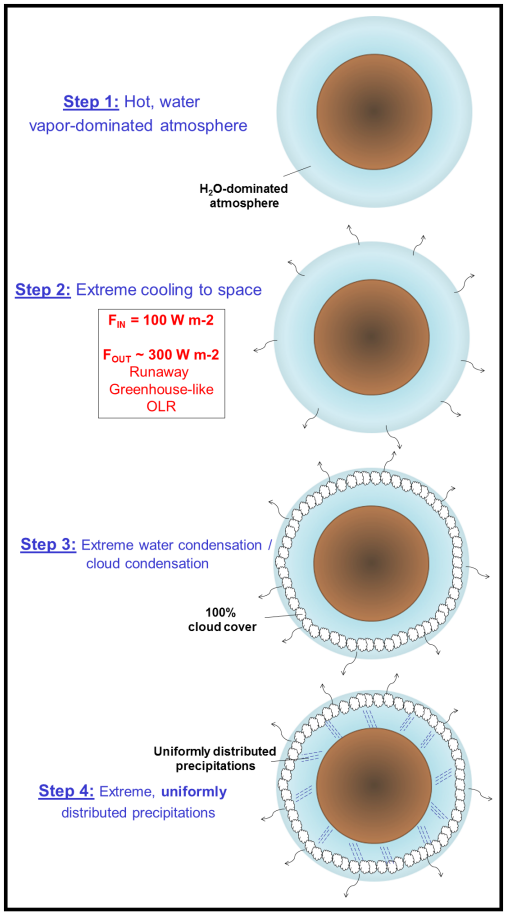

Figure 1: Sketches of the physical processes occuring after a post-impact hot, steam atmosphere forms on Early Mars.

Compared to previous studies [16,20-24,26], we carefully took here into account the radiative effect of spectroscopic features (far line absorptions and Collision Induced Absorptions) typical of CO_2-H_2O rich [29-31] post-impact atmospheres. In particular, we find that far-line IR opacities can be increased by 1-2 orders of magnitude, when broadening properly H_2O lines by CO_2 (instead of air). We will present the effect of these new spectroscopic refinements on the climate modelling of impact events at the 2017-EPSC conference.

3.2 Middle-size impact events

We estimate that moderate-size impact events (5km < $D_{impactor}$ < 50km, N_{events} ~ $3x10^3$ [32]) being much more numerous, they are potentially the best candidates to form the Noachian valley networks. They could in fact melt the ice that tends to accumulate preferentially in the regions where the rivers were sculpted ('Icy Highlands' scenario [16,25]). This scenario is particularly appealing because it would be an efficient mechanism of recharge of the valley network water sources between two impact-induced melting events.

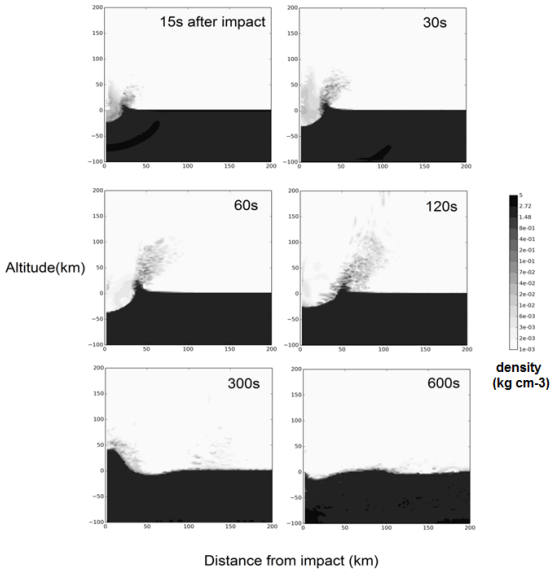

Figure 2: Time lapse of SOVA hydrocode simulations showing the volumetric density of materials following a ~15km diameter comet hitting Mars surface at 10km/s.

We will present preliminar estimates of the amount of rainfall/snowmelt that should be expected after impact events depending on their size, composition, velocity, … For this, we use the SOVA hydrocode [33] for short-term modelling of impact cratering. It provides us with post-impact temperature fields, injection of volatiles, ejecta and dust distribution (Fig 2) that serve as input for the LMD Generic Global Climate Model.

References

[1] Hynek et al. 2010, JGR. [2] Craddock & Howard 2002, JGR. [3] Mangold et al. 2012, JGR. [4] Grotzinger et al. 2015, Science. [5] Malin & Edget 2003, Science. [6] Moore et al. 2003, GRL. [7] Mangold & Ansan 2006, Icarus. [8] Poulet et al. 2005, Nature. [9] Bibring et al. 2006, Science. [10] Mustard et al. 2008, Nature. [11] Ehlmann et al. 2011, Nature. [12] Carter et al. 2013, JGR. [13] Carter et al. 2015, Icarus. [14] Haberle et al. 2017, Cambridge Univ. Press. [15] Forget et al. 2013, Icarus. [16] Wordsworth et al. 2013, Icarus. [17] Ramirez et al. 2014, Nature geoscience. [18] Batalha et al. 2015, Icarus. [19] Wordsworth et al. 2017, GRL. [20] Segura et al. 2002, Science. [21] Segura et al. 2008, JGR. [22] Segura et al. 2012, Icarus. [23] Toon et al. 2010, AREPS. [24] Turbet et al. 2017, Icarus. [25] Bouley et al. 2016, Nature. [26] Turbet et al. 2016, DPS. [27] Turbet et al. 2017, MAMO. [28] Kopparapu et al. 2013, ApJ. [29] Ma & Tipping 1992, J. Chemn. Phys. [30] Pollack et al. 1993, Icarus. [31] Baranov 2016, JQSRT. [32] Robbins & Hynek 2012, JGR. [33] Shuvalov 1999, Shock Waves.

EPSC Abstracts
Vol. 11, EPSC2017-658, 2017
European Planetary Science Congress 2017

Experimental Investigation of the Formation of Complex Craters

E. Martellato (1), M.A. Dörfler (2), B. Schuster (2), K. Wünnemann (1), and T. Kenkmann (2)
(1) Museum für Naturkunde, Leibniz Institute for Evolution and Biodiversity Science, Berlin, Germany, (2) Institute of Earth and Environmental Sciences, Geology, Albert-Ludwigs-University Freiburg, Germany (email: elena.martellato@mfn-berlin.de)

Abstract

The formation of complex impact craters is still poorly understood, because standard material models fail to explain the gravity-driven collapse at the observed size-range of a bowl-shaped transient crater into a flat-floored crater structure with a central peak or ring and terraced rim. To explain such a collapse the so-called Acoustic Fluidization (AF) model has been proposed [1]. The AF assumes that heavily fractured target rocks surrounding the transient crater are temporarily softened by an acoustic field in the wake of an expanding shock wave generated upon impact. The AF has been successfully employed in numerous modeling studies of complex crater formation [2, 3]; however, there is no clear relationship between model parameters and observables. In this study, we present preliminary results of laboratory experiments aiming at relating the AF parameters to observables such as the grain size, average wave length of the acoustic field and its decay time τ relative to the crater formation time.

1. Introduction

Impact craters have shaped the surfaces of planetary bodies since the formation of the Solar System, and the peculiarity of the process leading to their formation (high amount of energy release within a short time) makes them a natural tool to probe the interior of planetary bodies and reveal changes in density, strength, water content, porosity, composition, etc.

The initial transitional cavity resulting from shock-induced excavation flow (the so-called transient crater) is unstable in the given gravity field and undergoes modification (e.g. [4]). The subsequent collapse, which determines the final crater morphology, depends on the gravity field and target properties such as strength, composition, and layering, in addition to the crater size. When the crater diameter is larger than some critical threshold diameter D_{sc} that varies among planets with different surface gravities (e.g., D_{sc}~3-5 km on the Earth, ~15 km on the Moon, ~3-10 km on Mars, and ~10 km on Mercury), the transient cavity undergoes a distinct modification process, which includes uplift of the crater floor and underlying strata to form central peaks or peak rings, and failure of the rim into wide zones of stepped terraces. Such a collapse requires a stress field in excess of the failure strength of rocks to allow for plastic material flow.

1.1 Acoustic Fluidization

One current model invoked to explain such a collapse is the so-called Acoustic Fluidization (AF) model [1], which relies on the temporary softening of heavily fractured target rocks by means of an acoustic field in the wake of an expanding shock wave generated upon impact. The AF model assumes that the overburden pressure in heavily fractured material at some depth in the vicinity of the crater fluctuates due to high-pressure amplitude, high-frequency, random acoustic waves that exist in the wake of the expanding shock front. In the phase of temporary relieve of the overburden pressure the frictional resistance between fragments is reduced so that the fragments may easily shear against one another.

The Block Model (BM) [5] is a simplification of AF model that has been implemented in the iSALE shock physics code (http://www.isale-code.de). BM is described by two parameters: the kinematic viscosity of the fluidized region η, and the decay time of the block vibrations τ [5]. Theory suggests that both the viscosity η and the decay time τ are functions of the density ρ, block size h of the fragmented sub-crater rock mass, and period T of the

block oscillation. In turn it has been suggested [5] that the block length parameter *h* can be scaled by a quantity describing the transient cavity depth.
This study aims at a better understanding of the mechanics of complex crater formation, by (i) constraining BM parameters in relation to crater observables, (ii) improving the BM implementation into iSALE, and (iii) on coupling the BM with fragmentation models describing how intact rocks are turned into fragments, whose size varies according to the distance from the impact point. Here we present preliminary results of a series of laboratory experiments, where we tested the development of the complex morphology in acoustically excited granular targets.

2. Method

The laboratory setup is designed to study the whole impact process, including the fluidization of the target material causing mass movements into the cavity. The impact experiments we conducted with a 6.35 mm spring-driven air gun mounted perpendicular to the target surface, which accelerates plastic (density=1.4 g/cm3) projectiles to velocities as high as 180 m/s. The experiments were equipped with headlights and two LaVision Imager sCMOS cameras. The target is a box of fine-grained material, which is fluidized by acoustic vibrations through an external artificial source (speaker system). In fact, the natural generation of acoustic noise behind the shock wave is not possible due to the scale of the experiment, where the fluidization time is short relative to the time of crater collapse.

3. Results

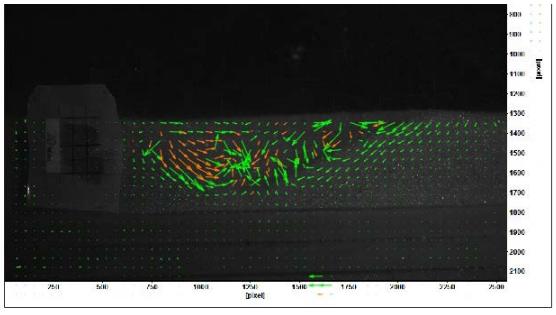

Figure 1: Particle displacement analysis for the shot of a plastic 6.35 mm projectile into a 420-840 µm glass beads target fluidized with frequency of 100 Hz.

We perform a systematic number of shots while varying the target grain size (~100-800 µm), and the frequency of the acoustic wave (50-500 Hz). The wavelength of the external acoustic wave is modulated to match the size of the particles. Particle displacements and strain of the collapse are analyzed through the Matlab tool “PIVlab” [6, 7, 8]. Figure 1 shows a cross section of the final stage of crater formation of a shot on a quarter space setup geometry, where the target is composed of glass beads (420-840 µm). The frequency of the acoustic field was set to 100 Hz.

4. Summary and Conclusions

We observe that the highest fluidization of the target material is achieved for low frequencies (100-200 Hz). A subtle displacement of grains at the crater floor can be observed, but no central peak arises. In the next shot campaign, we will investigate the influence of the wave amplitude for the development of the central peak.

Acknowledgements

This project has received funding from the European Union's Horizon 2020 research and innovation programme under the Marie Skłodowska-Curie grant agreement No 709122.

References

[1] Melosh, H.J.: Journal of Geophysical Research, Vol. 84, pp. 7513-7520, 1979.

[2] Bray, V.J. et al.: Meteoritics & Planetary Science, Vol. 43, pp. 1979-1992, 2008.

[3] Collins, G.S. et al.: Meteoritics & Planetary Science, Vol. 43, pp. 1955-1977, 2008.

[4] Melosh, H.J.: Impact Cratering: a geological process, Oxford Univ., 1989.

[5] Wünnemann, K. and Ivanov, B.A.: Planetary and Space Science, Vol. 51, pp. 831-845, 2003.

[6] Thielicke, W. and Stamhuis, E.J.: Journal of Open Research Software, Vol. 2, pp. e3, 2014.

[7] Thielicke, W. and Stamhuis, E.J.: PIVlab - Time-Resolved Digital Particle Image Velocimetry Tool for MATLAB, Figshare, 2014.

[8] Thielicke, W.: The Flapping Flight of Birds - Analysis and Application. PhD Thesis, 2014.

EPSC Abstracts
Vol. 11, EPSC2017-684, 2017
European Planetary Science Congress 2017

Geomorphometry of simple crater degradation classes on mare Serenitatis

V. Vivaldi (1,2), M. Massironi (2,1), A. Ninfo (3) and G. Cremonese (1)
(1) INAF-OAPD, Padua, Italy, (2) University of Padua, Dept. of Geosciences, Italy), (3) Dipartimento di Fisica e Scienze della Terra, University of Ferrara, Italy

Abstract

The classification of impact crater degradation is performed through a subjective visual interpretation of lunar surface images [1]. Here we propose an alternative quantitative methodology based on a morphometric analysis of simple impact craters carried out on high resolution digital terrain models (DTM). Our results have provided a quantitative distinction among different crater classes and have shown common trends of degradation, in function to diameter. The statistical analysis of crater morphometry allowed us to constrain the degradation classes in a 3D diagram that clearly shown a cluster distribution of the four degradation classes.

1. Introduction

In this study we have applied 3D morphometric analysis on high resolution DTMs, derived from LROC Narrow Angle Camera (NAC) that provide a resolution range from 0.5 to 2 m/pixel and Kaguya-Selene (JAXA), that provided a global DTM with a resolution of 7 to 10 m/pixel.
Morphometric analysis pointed to the calculation of the first two elevation derivatives (slope and curvatures) and their statistical distribution. In particular curvatures were retrieved by applying a multiscalar approach [4], in order to reduce DTM building and interpolation errors. Multiscalar approach was applied both to Kaguya TC DTMs and LROC-NAC DTMs. For the LROC NAC DTMs every kernel sizes from 3x3 to 99x99 were calculated. On LROC DTMs those kernel sizes correspond to windows sizes ranging from 6m2 to 198m2. The more favorable kernel resulted the 33x33 one, which coincides to a windows area of 66m^2, as shown in fig.1. For the Kaguya TC DTMs every kernel sizes from 3x3 to 33x33 were tested and the best size calculated was the 15x15 one, which corresponds to a 150m^2 window area (fig.1).

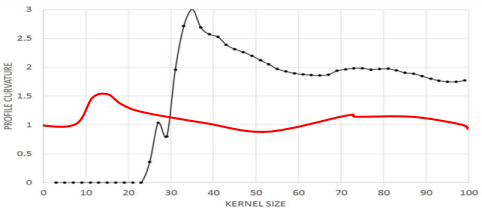

Figure 1: Plots of the maximum expression of the profile curvature at different evaluation kernel sizes for the LRO DTM (black line) and for the Kaguya DTM (red line), testing every kernel sizes from 3×3 to 99×99. For the LRO DTMs were estimated the peak of profile curvature expression on kernel 33, whereas for the Kaguya DTM on kernel 15.

2. Morphometric signature of a fresh impact crater

We firstly derived and measured the morphological expression of the four different crater domains (outer and inner wall, rim and floor) from a very fresh pristine crater. At this purpose we have chosen Linné crater, that is considered one of the best examples of pristine craters on the Moon [3].
The floor presents a mean slope gradient of 0°-3° with a profile curvature of 0.05°; those values are typical of a flat floor. The inner scarp has a mean slope gradient of 31.8°, consistently with the lunar regolith angle of repose (31°), whereas the mean profile curvature is 0.1°, suggesting a slightly convex morphology (> 0).
The most interesting result derives from the rim sector that presents a mean profile curvature of 0.5° (convex morphology), with a slim top area with about 0° of profile curvature and 0° of slope, revealing the presence of a pristine crest: this kind of features are typical of a very fresh crater.

On the outer scarp the mean slope gradient is about 10° and the profile curvature is negative (-0.05°), defining a slightly concave morphology.
Using Linné crater as a morphometric reference for the simple impact crater morphology we have conducted a morphometric analysis on the other three degradation classes (C2, C3, C4), in order to set up the characteristic thresholds of the four degradation classes. Afterwards we applied morphometric analysis on several simple craters on S28 geological unit within mare Serenitatis [2].

2. Morphometric comparison of the four degradation classes

Our results have provided a quantitative distinction among different crater classes and have shown common trends of degradation, going from larger to smaller craters within each class. Morphometric variables allowed the characterization of the morphometric signature of a very fresh impact crater. The resulting distribution of inner walls slope values shows a degradation trend within the first three. The first three degradation classes indeed follow a comparable power law trend: the mean slope increases from small to large diameters, as shown in the inner wall mean slope/diameter ratio diagram (Fig.6). C4 class is instead characterized by a wide dispersion of the data. The distribution of the negative profile curvature values follows a similar power law trend for C1 and C2, which becomes less defined for C3 and disappear in C4. This enlightens how the concavity along the inner wall tends to decrease in function of degradation class from C1 to C4, according with a flattening morphological evolution from less degraded to more degraded craters.
To improve the statistical significance, we have considered also the rim crater sector. We extracted the profile curvatures from craters rim in order to understand the morphological evolution of this feature. We found that the morphological degradation trend of rim and inner wall is comparable so we were able to plot in a 3D diagram rim and inner wall in function to diameter.
The resulting distribution shown a well clustered distribution of the four degradation classes, allowing us to consider it as an objective distinction of the degradation classes (fig 2).

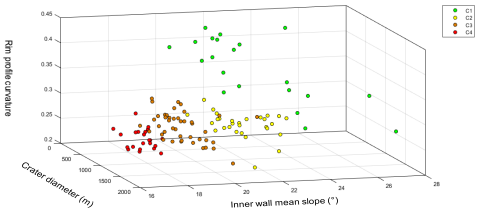

Figure 2: 3D plot of rim profile curvature, inner wall mean slope and diameter.

3. Summary and Conclusions

In this research we have applied morphometric analysis on high resolution topographic data in order to quantify the degradation of simple impact craters. The statistical distribution of the inner wall mean slopes highlighted a similar power law trend of the first three degradation classes, which seems independent from the degradation class. The development of morphometric variables classification described in this research, may be also useful for semi-automatic detection and characterization of the degradation classes of simple craters, potentially helpful for geological mapping and age determination of planetary surfaces.

Acknowledgements

This research was supported by the Italian Space Agency (ASI) within the SIMBIO-SYS Project (ASI-INAF agreement no. I/022/10/0).

References

[1] Arthur, D.W.G., Agnieray, A.P., Horvath, R.A., Wood, C.A., Chapman, C.R.: The system of lunar craters. Quadrant I. Comm. Lunar Planet. Lab. 2, #30, 1963.
[2] Hiesinger, H., Head, J.W., Wolf, U., Jaumann, R. and Neukum, G.: Ages and stratigraphy of lunar mare basalts: A synthesis. Geological Society of America Special Papers 2011;477;1-51 doi: 10.1130/2011.2477(01), 2011.
[3] Martellato, E., Vivaldi V., Cremonese G., Massironi M., Ninfo A., Marzari F., Haruyama J.: Is Linné morphology influenced by the lunar stratigraphy? Insights from numerical modeling. Meteoritics & Planetary Science, ISSN: 1945-5100 - Accepted 2017.
[4] Wood, J.: The geomorphological characterization of digital elevation models. PhD Thesis, University of Leicester, UK, 1996.

EPSC Abstracts
Vol. 11, EPSC2017-716-1, 2017
European Planetary Science Congress 2017

The post-impact metamorphism textures of various type meteorites

V. Grokhovsky, R. Muftakhetdinova, E. Petrova, and G. Yakovlev
Ural Federal University, Institute of Physics and Technology, Ekaterinburg, Russia
(grokh47@mail.ru)

Abstract

In this paper, a review of the features of shock metamorphism in stony and iron meteorites is given on the examples of Chinga and Sikhote-Alin iron meteorites before and after high-intensity shock loading; and Chelyabinsk LL5, Tsarev L5 chondrites.

1. Introduction

The study of extraterrestrial substance in recent years has been given a special attention. This is due to both the activation of planetary missions for the small bodies exploration in the Solar system, and increasing amount of newly discovered meteoritic samples. Shock waves are an integral part of the extraterrestrial matter evolution processes. Kinetics and mechanism of phase and structural transformations in this material influenced by the shock waves. It is possible to obtain a wide range of these transformations in a one sample during the converging waves loading experiment [1].

2. Samples and methods

A series of experiments on shock wave loading were performed on the fragments of Chinga IVB, Sikhote-Alin IIAB, Chelyabinsk LL5 and Tsarev L5 meteorites [2-5]. Samples and conditions for their low- and high-intensity explosive loading in the laboratory experiments are presented in [2, 3]. Microstructure studies were carried out using the Zeiss Axiovert 40 MAT optical microscope and scanning electron microscopy Carl Zeiss Σigma VP with energy dispersive spectroscopy (EDS) and electron backscattering diffraction (EBSD) units.

3. Results and discussion

A spherical central cavity of the ball from the Chinga meteorite was formed after the explosive loading. It is explained by realized conditions of the high-speed high-intensity loading and the fact that Chinga ataxite have a quasi-isotropic macrostructure. The formation of adiabatic shear bands and regions of localized material flow. It should be noted that the Schlieren bands on the surface of Chinga sample both in the initial substance and after shock experiments were observed (fig.1).

Figure 1: Sector of the ball from the Chinga meteorite after shock wave loading (diameter 56.01 mm).

Because of it heterogeneous texture of the Sikhote-Alin sample in the central part the distribution of cracks and discontinuities is not spherical (fig.2). The features of shock metamorphism were observed in the Sikhote-Alin iron meteorites, such as traces of $\alpha \rightarrow \varepsilon \rightarrow \alpha$ transformations in kamacite, $\alpha \rightarrow \gamma \rightarrow \alpha_m$ massive transformation in kamacite, contact melting zones at the rhabdite – kamacite boundary, and complete remelted phosphide regions. It was shown that the polycrystalline texture of the contact melting zone was formed by the bcc phase that was supersaturated solid solution of phosphorus in the α-Fe(Ni) [6]. It was determined that the nature and distribution of deformation defects and areas with traces of $\alpha \rightarrow \varepsilon \rightarrow \alpha$ transformation along the radius of the spherical sample are under the influence of the geometry of the shock-wave action and the original

macro- and microstructure of the meteorite. EBSD and the local X-ray analysis clearly show that Fe-Ni alloy of meteoritic origin after action of an explosive spherical compression contain areas undergoing polymorphic α→ε and ε→α transitions [1,6].

Figure 2: Cross-section of a ball from the Sikhote-Alin meteorite after shock wave loading (diameter 50.00 mm).

Previously, the studies of Saratov L4 meteorite by spherical shock waves loading demonstrated immiscible silicate and sulfide melts, redox reactions and effect of anomalous mass transfer [2-4]. In contrast to porous material of Saratov L4, which were partly destroyed after the shock experiment, Tsarev L5 material were saved. Shock loading of the Tsarev L5 provide a wide range of temperature and pressure effects. Radial disposing of textural shock effects within the material refers to increment of the shock intensity from the sample surface to the center. As the result, zones of deformation, melting and partial melting of the material were developed after shock experiments with chondritic material. Estimation of the internal structure transformation was done. Shock features in the Tsarev L5 meteorite material of the different shock level was obtained as the result of the experimental shock. As initial material in the outer part of the sample as completely melted material in the central part can be observed. Furthermore, it is possible to compare experimentally created textural shock features with original material and melted parts of the Tsarev meteorite breccia material.

4. Summary and Conclusions

Possible structural changes in the meteorite matter formed with significant peak pressures and temperatures were demonstrated as the result of simulation experiments. Experimental conditions allow one to obtain the range of effects in the testing substance from the plastic deformation to the complete melting.

Acknowledgements

This work was supported in part by the Ministry of Education and Science of the Russian Federation (Project no. 3451, 4825) and the Act 211 of the Government of the Russian Federation, agreement no. 02.A03.21.0006.

References

[1] Muftakhetdinova R.F. et al. An effect of contact melting in the Sikhote-Alin iron meteorite after isentropic spherical shock waves loading, Letters on materials Vol. 5(1), pp. 110-114, 2015.

[2] Kozlov E.A., Zhugin Y.N., Litvinov B.V. et al. Features of physicochemical transformations of chondrites "Saratov" in spherical shock waves, DAN, Vol. 353 (2): pp. 183-186, 1997.

[3] Kozlov E.A., Zhugin Yu.N., Litvinov B.V. et al. In: Abstracts of Int. Conf. Shock Waves in Condensed Matter, July 12-17,1998, St.−Petersburg., Russia, pp. 182—183, 1998.

[4] Rusakov V.S., Kupin Y.G., Badyukov D. D. et al. State of Fe atoms in minerals of the Saratov chondrite affected by spherical impact waves, Geochemistry International, pp. 300—303, 1998.

[5] Gizzatullina R. F., Grokhovsky V.I., Yakovlev G.A.. The structural changes in the kamacite-rhabdite boundary regions of shock loaded Sikhote-Alin iron meteorite, Meteoritics & Planetary Science. Vol. 49 (SI) pp. A137

[6] Muftakhetdinova R.F., Grokhovsky V. I., Kozlov E. A., Khomskaya I. V., Yakovlev G. A., Phase transformation α→ε in meteoritic Fe – Ni alloy under shock-wave loading, Technical Physics. Vol. 61 (12), pp. 1830–1834, 2016.

EPSC Abstracts
Vol. 11, EPSC2017-812, 2017
European Planetary Science Congress 2017

Radiation and ablation of large meteoroids decelerated in the Earth's atmosphere

D.O. Glazachev, O.P. Popova , E.D. Podobnaya, V.V. Svetsov and V.V. Shuvalov
Institute for Dynamics of Geospheres RAS, Moscow, Russia (olga_idg@rambler.ru / Fax: +7-499-1376511)

Abstract

Radiative fluxes caused by the impacts of asteroidal and cometary bodies of various sizes (20-100 m) were determined by systematic modeling. Scaling relations, which allow to estimate energy of thermal radiation, ablation efficiency and to approximate radiative fluxes on the Earth's surface are suggested.

1. Introduction

When cosmic bodies of asteroidal and cometary origin, with sizes from 20 to approximately 100 m, enter dense atmospheric layers, they are destroyed with a large probability under the action of aerodynamic forces and decelerated with the transfer of their energy to the air at heights from 20–30 to several kilometers. Earlier, numerical simulations of the disruption (with allowance for evaporation of fragments) and deceleration of similar meteoroids entering the Earth's atmosphere at various angles were performed, and the heights of an equivalent explosion point generating the same shock wave as the fall of a cosmic body with given parameters were determined [1].

Thermal radiation is one of the main hazardous factors in the impact scenarios, which could result in fire ignition over large areas. The famous Tunguska cosmic body was responsible for fires on the area of 200-500 km^2 [2]. For quick evaluation of thermal radiation, scaling relations are needed, which allow to estimate thermal exposure and thermal fluxes from assumed properties of an impactor. The point source approximation may be useful for quick estimates of thermal damage, but the position, effective altitude of the source and integral luminous efficiency should be determined. Besides, the fireballs can significantly differ in shape from point explosions, and corresponding radiation field can be heterogeneous.

Recently, systematic modeling of the entry of asteroidal and cometary bodies of different sizes (20-3000 m), including the determination of thermal fluxes and exposures, was carried out [3]. Results of these simulations provide an opportunity to derive scaling relations for thermal radiation characteristics as well as ablation efficiency.

2. Thermal exposure and its approximation

Radiation fluxes were calculated by integrating the equation of radiative transfer along rays passing through a luminous area taking into account spectral dependence of radiation in a multigroup approximation [3]. An example of radiation exposure distribution on the surface is given in Fig. 1 for a 30 m comet entering the atmosphere with a 20 km/s velocity at an entry angle of 45 degrees. The thermal energy distribution on the surface demonstrates a deviation from circular symmetry, which could be expected in the case of a point source.

Analyzes of simulation results permit to suggest scaling relations, which allow to estimate irradiated energy and to approximate radiative fluxes on the surface. These relations are dependent only on cosmic body density, size, velocity and angle of entry. Two variants of application of scaling relations are shown in Fig. 1 in comparison with the result of numerical modeling. The inclusion of heterogeneity of the radiation field to the approximation allows us to obtain better agreement.

The integral luminous efficiencies are shown in Fig. 2 versus kinetic energies of bodies with energies 0.6 – 450 Mt entering the atmosphere at different angles. The efficiency of radiation varies from several percent to 10-20%, and is dependent on kinetic energy, entry angle and other parameters. In most cases an uncertainty in estimates based on the scaling relations does not exceed 10-20%, in all cases this uncertainty is smaller than 60%. As an example, a dashed line shows scaling relation estimates for the asteroids entering the atmosphere at 45^0.

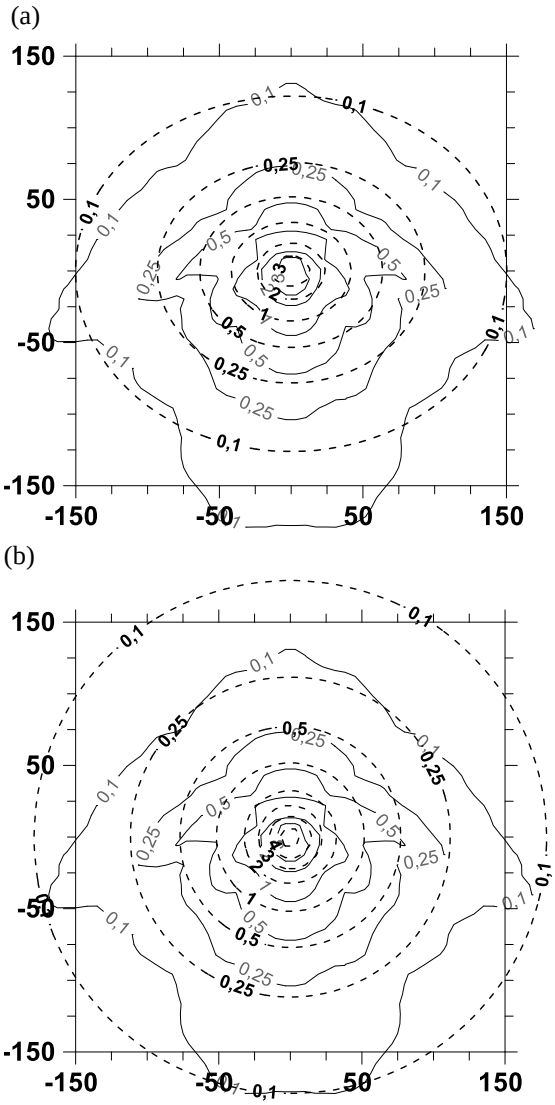

Figure 1: Distribution of radiative exposure (exposure values are given on contour lines in J/cm^2) on the surface for a 30 m cometary body that entered the atmosphere with velocity 20 km/s and entry angle 45^0. Solid lines represent corresponding numerical simulations, dashed lines demonstrate application of simplified approximations, taking into account the heterogeneity of the radiation field (a) and without it (i.e. point source approximation) (b). The axes correspond to distance in km, the trajectory is directed from below upwards, maximum luminosity point is in the point of origin of coordinates.

3. Summary

Radiative fluxes caused by the impacts of asteroidal and cometary bodies of different sizes (20-100 m) have been determined by the systematic modeling. Simplified approximations, which allow to estimate radiation energy and to describe the radiative fluxes on the surface as well as ablation efficiency, are suggested.

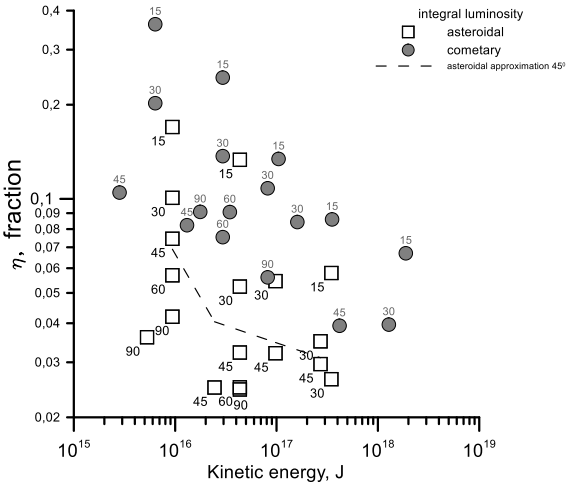

Figure 2: Integral luminous efficiency versus kinetic energy of asteroidal and cometary objects (entry angles are labelled). Dashed line corresponds to suggested scaling relation for the cases with an entry angle of 45^0.

Acknowledgements

This work was supported by the Russian Science Foundation, project no. 16-17-00107.

References

[1] Shuvalov V.V. et al.: (2016) Sol. Syst. Res., 50, 1–12, 2016.

[2] Svetsov, V.V.: Comment on “Extraterrestrial impacts and wildfires”, Palaeogeogr. Palaeoclimatol. Palaeoecol., Vol. 185, pp. 403-405, 2002.

[3] Svetsov, V.V., Shuvalov V.V.: Thermal radiation from large bolides and impact plumes. Abstract (this conference).

EPSC Abstracts
Vol. 11, EPSC2017-881-1, 2017
European Planetary Science Congress 2017

Impact Effects Calculator. Orbital Parameters.

S.A. Naroenkov(2), D.O. Glazachev(1), A.P. Kartashova(2), I.S. Turuntaev(1), V.V. Svetsov (1), V.V. Shuvalov(1), O.P. Popova(1) and E.D. Podobnaya(1)
(1)Institute for Dynamics of Geospheres RAS, Moscow, Russia (glazachevd@gmail.com / Fax: +7-499-1376511),
(2)Institute of Astronomy RAS, Moscow, Russia

Abstract

Next-generation Impact Calculator for quick assessment of impact consequences is being prepared. The estimates of impact effects are revised. The possibility to manipulate with the orbital parameters and to determine impact point is included.

Introduction

The population of near-Earth objects (NEOs, both asteroids and comets) contains a wide variety of bodies with diverse physical and dynamical properties, and presents a permanent threat to our civilization [1]. The number of undiscovered potentially hazardous asteroids with sizes from 140 meters to 1km is estimated as about 20 000 objects, the number of potentially dangerous bodies with sizes from 50 m to 140 m is estimated to exceed 200 000 objects [2]. The recent Chelyabinsk event demonstrated that even a small object, only 20 m in diameter, has enough energy to cause considerable destruction of property.

1. Impact calculator

Detection of new objects proceeds continuously. The characteristics and orbital parameters of an already discovered body are also regularly refined. For any discovered object it is necessary to assess the potential risk and damage resulting from the possible collision of such body with the Earth. Physical processes, which occur during the impact, are complex and their simulations are time consuming. An instrument for quick estimation of the consequences of a comet or asteroid impact on the Earth is needed. Such Web-based calculator was created by Collins et al [3].

We are going to elaborate the next generation version of an impact calculator. Extensive numerical simulations of impacts are carried out using a hydrodynamic model, equations, and a numerical technique described, e.g., in [4]. It is assumed that the cosmic object has no strength, deforms, fragments, and vaporizes in the atmosphere. After the impact on the ground, formation of craters and plumes are simulated. Results obtained in these simulations will be used to get interpolations for rapid assessment of the impact effects. As an example, in the calculator [3] thermal damage from crater-forming impacts is considered based on nuclear explosions results and crater plume luminous efficiency estimates but the radiation from the objects decelerated in the atmosphere is not included [3]. For our calculator, the systematic modeling of the entry of asteroidal and cometary bodies of various sizes (20-3000 m), including the determination of thermal fluxes and exposures, was carried out [5], and scaling relations for thermal fluxes on the ground were found [6]. These and other similar scaling relations will be used for fast online estimates of impact effects in our calculator. These relations are dependent only on cosmic body density, size, velocity and angle of entry.

To predict impact effects in any location one must determine the place of the impact (or the point of maximum energy deposition) or to find it based on suggested orbital parameters of the impacting object. So we decided to include an orbital block into our calculator.

2. Orbital characteristics and impact point

Our impact consequences calculator allows to create a virtual (hypothetical) orbit of the celestial body, which will lead to a collision with the Earth. The impact point may be determined based on this orbit. The creation of a virtual orbit can be realized by two ways.

In the first way, the user, setting five parameters of the Keplerian orbit, the date of collision, the size of the object, creates a dangerous orbit and collision conditions. For the first method, the place, speed and energy of the collision are predicted. The second way allows to predict a dangerous orbit based on the time and place of collision, the angle of entry into the atmosphere, the direction and speed of the impact. We

believe that both possibilities can be interesting and in demand.

To determine the orbit, a numerical model is used, which takes into account perturbations from the Earth, the Moon, the Sun, the rotation of the atmosphere, and the resistance of the atmosphere. This numerical model was tested at the orbits of such bodies as the Chelyabinsk meteorite [7], 2008 TC3, Novato meteorite [8], meteoroid 2014 AA.

For the parameters of Chelyabinsk meteoroid orbit [7], we determined the flight trajectory. The coordinates of the largest meteorite fall site were compared with the projection of our predicted trajectory on the Earth's surface. The distance between the fall and our trajectory was 600 meters. These results confirmed the correctness of the numerical model for the orbit and the impact point determination. We also studied the circumstances of the fall of known asteroids, which can hypothetically collide with the Earth. For the study, 27 near-Earth asteroids were selected, in which the minimum distance between the orbit of the asteroid and the orbit of the Earth is less than 6378 km. We determined that most of the collision occurs at speeds of 15 to 25 km/sec, the angle of incidence on average is 45 degrees.

3. Summary

Next-generation Impact Calculator for quick assessment of impact consequences is being prepared. The estimates of impact effects are revised. The possibility to manipulate with the orbital parameters and to determine impact point is included.

Acknowledgements

This work was supported by the Russian Science Foundation, project no. 16-17-00107.

References

[1] Harris A. W., Boslough M., Chapman C. R., Drube L., Michel P., and Harris A. W. (2015) Asteroid impacts and modern civilization: Can we prevent a catastrophe? In Asteroids IV (P. Michel et al., eds.), pp. 835–854. Univ. of Arizona, Tucson.

[2] Committee to review near-Earth object surveys and hazard mitigation strategies. Defending planet Earth: Near-Earth object surveys. The National Academies Press, 152 p. 2010.

[3] Collins G.S., Melosh H.J., Marcus R. (2005) Earth Impact Effects Program: A Web-based computer program for calculating the regional environmental consequences of a meteoroid impact on Earth // Meteorit. Planetary Sci. V. 40. Nr.6. P.817-840

[4] Shuvalov, V.V., Svettsov, V.V., Artem'eva, N.A., Trubetskaya, I.A., Popova, O.P., and Glazachev, D.O.: Asteroid Apophis: Evaluating the impact hazards of such bodies, Sol. Sys. Res., Vol. 51, pp. 44-58, 2017.

[5] Svetsov, V.V., Shuvalov V.V.: Thermal radiation from large bolides and impact plumes. Abstract (this conference).

[6] Glazachev D.O., Popova O.P., Podobnaya E.D., Svetsov V.V. and Shuvalov V.V.: Radiation and ablation of large meteoroids decelerated in the Earth's atmosphere. Abstract (this conference).

[7] Emelyanenko V.V., Naroenkov S.A., P. Jenniskens, O. P. Popova. The orbit and dynamical evolution of the Chelyabinsk object. // Meteoritics & Planetary Science, 2014, V. 49, Is. 11, p 2169- 2174

[8] Jenniskens, P et al,. Fall, recovery, and characterization of the Novato L6 chondrite breccia. METEORITICS & PLANETARY SCIENCE, Volume: 49, Issue: 8 Pages: 1388-1425

EPSC Abstracts
Vol. 11, EPSC2017-912, 2017
European Planetary Science Congress 2017

New Insights into Shatter Cone Formation from MEMIN Experiments

J. Wilk (1), T. Kenkmann (1), and C. Hamann (2)
(1) Institute of Earth and Environmental Science-Geology, Albert-Ludwigs-University Freiburg, Freiburg, Germany,
(2) Museum für Naturkunde, Leibniz-Institut für Evolutions- und Biodiversitätsforschung, Berlin, Germany
(jakob.wilk@geologie.uni-freiburg.de)

Abstract

We recovered shatter cone fragments from the ejecta of hypervelocity impact experiments, performed in the framework of MEMIN. The fragments geometries were characterized by WLI, and the fractures surfaces themselves by SEM. We estimated low bulk shock pressures of 2 to 5 GPa for the material in which the shatter cones have formed. The microstructural investigation revealed intricate melt films and shear deformation along the shatter cone surface, indicating increasing strain towards the same. Combining our observations with a possible formation model, we interpret shatter cones as the result of symmetric crack branching of rapidly propagating fractures with a resulting mixed mode I/II fracture surface.

1. Introduction

Shatter cones are the only macroscopic shock effect, diagnostic for the recognition and verification of impact structures. Nonetheless, their formation and the physical boundary conditions are still subject of debate [1]. To narrow down the formation conditions of shatter cones, we systematically analyzed hypervelocity experiments conducted in the framework of MEMIN.

2. Shatter Cones in MEMIN

We recovered 24 shatter cone fragments from the mesoscale MEMIN experiments with 20–80 cm sized target cubes of sandstone, quartzite and limestone [2]. Experimentally produced shatter cones were found as fragments of 1.2 to 9.3 mm size in the ejecta and were delivered from the inner crater zone of pervasive grain crushing and compaction [3], which is easily identifiable in most of the MEMIN craters. The width of this area showed a range of 15–38% of the apparent crater diameter, which correlates with a minimum of 2 GPa shock pressure.

We obtained morphometric data from the recovered fragments by means of white-light-interferometry (WLI). In combination with laser scanning data of natural shatter cone samples, we studied apical angles and curvatures and developed a phenomenological model [4].
The SEM analyses of the recovered MEMIN fragments gave the opportunity to study intricate melt films preserved on the fresh shatter cone surfaces. We found both vesicular and polished melt films, decorated by micro-spherules. Subjacent to the melt films are zones of fragmentation and brittle shear, indicating movement away from the shatter cone apex of the rock that surrounds the cone. Smearing and extension of the melt film indicates subsequent movement in opposite direction to the comminuted and brecciated shear zone.

3. Formation Model

The microstructural investigation documents that fracturing, formation of smooth melt films and vesicular melts can be associated to the shock loading and unloading phase. We suggest that deformation along shatter cone surfaces does form as a succession of deformation events: Phase 1: Fragmentation and brittle shearing, along with fracture bifurcation, timed with the passage of the elastic precursor. Phase 2: Continued shearing under enhanced confinement and shock conditions. Frictional melting occurs within a narrow zone along the shatter cone surface. Smooth polished melt films and shock effects develop. Phase 3: Onset of pressure release leads to progressive melt production. Reverse shearing results from a release of stored elastic energy of the rock during unloading. Phase 4: Tensile fracture separation continues during unloading, but reverse shear movement decays. Microstructures that are associated with this final stage include vesicular textures without a preferred orientation/alignment of vesicles.

5. Figures

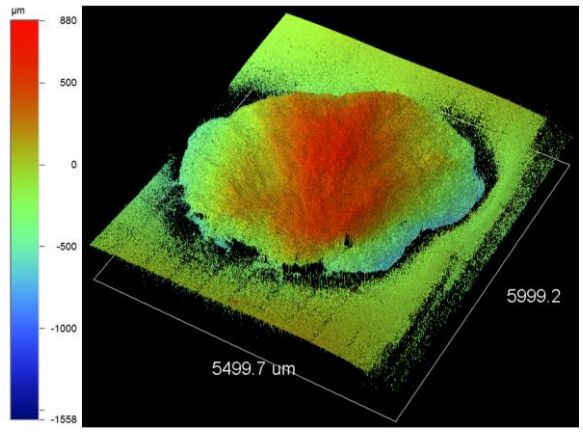

Figure 1: WLI scan of recovered shatter cone fragment from MEMIN experiment A15 (5 mm aluminum projectile shot on a 20 cm sized cube of sandstone at 6.97 km/s).

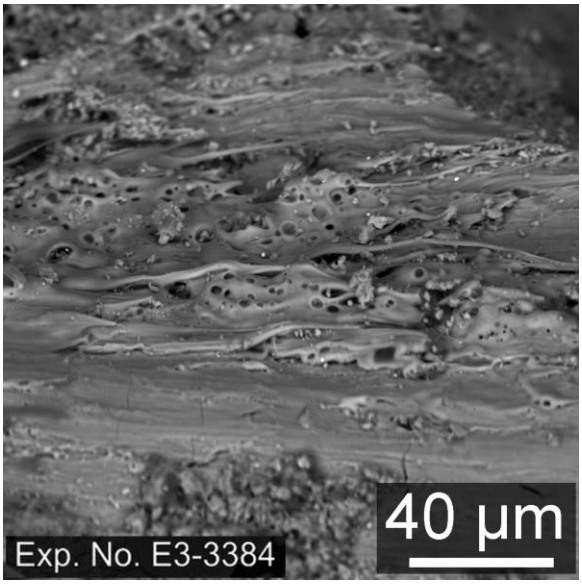

Figure 2: SE images of a shatter cone surface from experiment MEMIN E3 (12 mm Campo del Cielo projectile shot on an 80x80x50 cm sized target block of water saturated sandstone at 4.59 km/s).

6. Conclusion

We envisage shatter cones are build up by numerous cycles of fracture bifurcation early in the cratering process. Crack branching is the result of rapid fracture propagation that may approach the Raleigh wave speed. In experiments, shatter cones can be formed under low bulk shock conditions and still show intricate melt films along the fracture surface. Those melt films are formed by a combination of frictional heating and shock and infer that shatter cone surfaces are mixed mode I/II fracture surfaces.

Acknowledgements

This work is part of the DFG research unit FOR-887: “Experimental Impact Cratering: The MEMIN program” grants KE 732/22-1 and He-2893/8-2.

References

[1] Baratoux, D., and Reimold, W.U.: The current state of knowledge about shatter cones: Introduction to the special issue, Meteoritics and Planetary Science, Issue 8, pp. 1389-1434, 2016.

[2] Wilk, J., and Kenkmann, T.: Formation of shatter cones in MEMIN impact experiments, Meteoritics and Planetary Science, Issue 8, pp. 1477-1496, 2016.

[3] Buhl, E., Poelchau, M. H., Dresen, G., and Kenkmann, T.: Deformation of dry and wet sandstone targets during hyper-velocity impact experiments, as revealed from the MEMIN program, Meteoritics and Planetary Science, Issue 48, pp. 71–86, 2013.

[4] Kenkmann, T., Hergarten, S., Kuhn, T., and Wilk, J.: Formation of shatter cones by symmetric crack bifurcation: Phenomenological modeling and validation, Meteoritics and Planetary Science, Issue 8, pp. 1519-1533, 2016.

EPSC Abstracts
Vol. 11, EPSC2017-934, 2017
European Planetary Science Congress 2017

The real diameter of the Neugrund impact structure (Gulf of Finland, Estonia)

K. Suuroja (1), **S. Suuroja** (1) and Tom Floden (†) (2)

(1) Geological Survey of Estonia (s.suuroja@egk.ee / Fax: +372-6720091), (2) Stockholm University

Please make sure that your pdf conversion results in a document with a page size of 237 x 180 mm!

Abstract

The Neugrund impact structure is located on the southern side of the entrance of the Gulf of Finland (59°20' N, 23°31' E), immediately eastward of the Osmussaar Island (in Swedish Odensholm, what means Odin's Grave in English). The Neugrund impact structure was formed in Early Cambrian (about 535 Ma) as the result of impacting a chondritic asteroid about 1 km in diameter.

The Neugrund impact structure is the world´s best preserved meteorite crater in the sea, because almost all of its structures are preserved, exposed partly on seabed and they are easily accessible for the researchers. Neugrund is a complex meteorite crater about 19 km in diameter. In the center of the structure emerges the inner crater with quite narrow (ca 200 m) rim wall, which has about 6,5 km rim-to-rim diameter. The presence of central peak (uplift) in the crater, deep about 5,5 km diameter, is not proven. The 4–5 km wide terrace or zone of dislocations surrounds the inner crater.

The real diameter of the Neugrund impact structure has been under discussion since of revealing of the meteoritic origin of the structure in 1995. Several dimensions has been proposed, as 7 up to 20 km. Considering methodology used for determination of diameter of the quite similar impact structures (Gosses Bluff in Australia Ma 14,5 and Ries Nördligen in Germany Ma 14,5), ratio of diameter of the structure to the inner crater is approximately 3 km (accordingly 22 to 6 km and 24 to 8 km). In both cases, as by the Neugrund case, the limit of the structure is not clearly developed. In the Neugrund case the outer limit of the impact structure is marked by the unclearly developed ring fault outer which the sedimentary target rocks of the structure are intact. It follows from the foregoing dimensions of the Neugrund impact structure: rim-to-rim diameter of the inner crater – 6,5 km; diameter of the impact structure – 19 km, ratio of diameter of the structure to the diameter of the inner crater – 2,9.

Seismic reflection profiling (SRP) was one of the most commonly applied methods in investigation of the submarine Neugrund impact structure and it was the first method that cleared up the elements of the partially buried impact structure. The filtered bands 250–500 Hz were more suitable for revealing deeper buried bedrock layers and for surface of crystalline basement rocks, while filtered band 4 kHz was used for observing the buried bedrock surface under the Quaternary deposits and for revealing the details inside the latter. A disturbing circumstance was presence of thicker layers of Quaternary deposits containing gas (especially varved clays), which could not be penetrated by the wave of higher frequency bands (4 kHz).

Simultaneously with SRP the side-scan sonar (SSS) profiling was carried out for studding sea floor topography and a certain amount its sediment composition were surveyed within 100–400 m wide band. By the SSS profiling was established origin of the mega-blocks consisting of crystalline basement rocks and giant erratic boulders discovered in rather deep (more than 50 m) sea within the Osmussaar Deep westward of the Neugrund Bank and on other sites. The intensity of rebounded beam made possible deciphering lithological composition of a seabed.

EPSC Abstracts
Vol. 11, EPSC2017-987, 2017
European Planetary Science Congress 2017

Marine resurge sequences in drill cores from Flynn Creek impact structure, Tennessee, USA.

L. de Marchi (1), **J. Ormö** (2), D.R. Adrian (1), and D.T. King Jr. (1)
(1) Geosciences, Auburn University, Alabama USA (lzd0034@auburn.edu), (2) Centro de Astrobiología (INTA-CSIC), Spain (ormoj@cab.inta-csic.es).

Abstract

The Flynn Creek impact structure, a Late Devonian marine-target crater, contains a moat-filling sequence of normal graded beds (~ 30 m) that lie atop chaotic (slump?) breccia deposits. The present report focuses on the graded beds, including their granulometric characteristics and interpreted marine-resurge origin.

1. Introduction and aim of study

Roddy [1-4] first presented evidence that the Flynn Creek impact structure is a Late Devonian, 3.8-km diameter, complex impact crater, which formed in an epicontinental shelf sea. These early works by Roddy established Flynn Creek as the first interpreted marine-target impact crater on Earth. The Flynn Creek impact structure is located in north-central Tennessee USA (36° 17' N; 85° 40' W) and is well exposed at the surface. The crater has a terraced rim with an asymmetric ("pear-shaped") outline (Fig. 1), and displays a central uplift surrounded by a breccia-filled crater moat [4-6]. The target stratigraphic section was nearly flat-lying, mostly poorly consolidated, Upper Ordovician carbonates ranging from Knox Group through Catheys-Leipers Formation [4-6]. Almost all rim exposures consist of Catheys-Leipers Formation, whereas the central uplift exposures consist primarily of Knox and Stones River Groups [4-6]. Central uplift-flanking breccias are mainly coarsening upward slump deposits [7], whereas the upper moat shows normal graded breccias (this study). Upper Devonian Chattanooga Shale deposition had likely begun at the time of impact, but comprised a very thin, poorly consolidated target layer. The main phase of Chattanooga deposition is the regional post-impact deposit [4-6, 8].

2. Methods

Analysis of two drill cores, one in the northeastern moat area (FC77-3) and one in the southwestern moat area (FC67-3) was completed using granulometric line-logging and statistical analysis following the method applied to similar deposits in Lockne, Tvären, and Chesapeake Bay (CBIS) marine-target impact craters [9, 10].

3. Results and discussion

On the northeastern side of the moat (FC77-3) the complete breccia sequence is ~ 35 m thick, whereas on the southwestern side (FC67-3) it is ~ 112 m. Results presented here focus on the upper graded beds, which comprise the upper ~30 m in both drill cores. Our line-logging shows that both drill cores contain thick sequences of chaotic (slump?) breccia with overlying normal graded beds (Figs. 2&3). In both cores, the grain size (φ=-1*Φ) decreases upward in the upper part, whereas the sorting is improving (i.e., a lowering of the standard deviation σ of φ). With upward fining, there is also a steep increase in the number of clasts per meter until the effect of the applied cut-off grain size ≤5mm becomes visible at 11.5m and 23.5m respectively (Figs. 2-4). These patterns are consistent with other suspension flow resurge deposits overlying more chaotic material moved by traction as seen at Lockne, Tvären and CBIS [9, 10].

4. Conclusions

Our data set from the upper ~ 30m of both crater-moat drill cores shows tell-tale sedimentological characteristics of water-rich marine resurge deposition in which particles entrained in the return flow of water were deposited during the early modification stage of the marine impact event.

References

[1] Roddy, D.J.: *The Paleozoic crater at Flynn Creek, Tennessee*, Ph.D. thesis, Cal Tech, 1966. [2] Roddy, D.J.: In *Shock Metamorphism of Natural Materials*, Mono Book Corporation, Baltimore, pp. 291-322, 1968. [3] Roddy, D.J.: In *Impact and Explosion Cratering*, Pergamon, New York, pp. 277-308, 1977. [4] Roddy, D.J.: LPSC X Abstracts, pp. 2519-2534, 1979. [5] Evenick, J.C.: *Field Guide to the Flynn Creek Impact Structure*, U. Tennessee, Knoxville, 2006. [6] Gaither, T.A., et al.: LPSC XLVI Abstracts, #2089, 2015. [7] Adrian, D.A., et al. Meteoritics and Planetary Science, Vol. 52 (in press), 2017. [8] Schieber, J., and Over, D.J.: In *Understanding Late Devonian and Permian-Triassic Biotic and Climatic Events: Towards an Integrated Approach*, Elsevier, New York, pp. 51-70, 2005. [9] Ormö, J., Sturkell, E., and Lindström, M.: Meteoritics and Planetary Science, Vol. 42(11), pp. 1929-1944, 2007. [10] Ormö, J., Sturkell, E., Horton, J.W., Jr., Powars, D.S., and Edwards, L.E.: Geological Society of America Special Papers, Vol. 458, pp. 617-632, 2009.

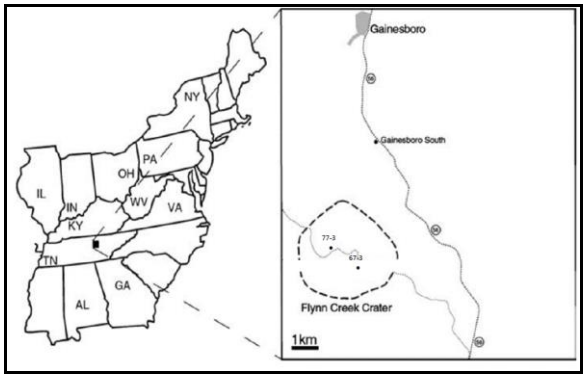

Figure 1. Map of the eastern USA; Tennessee is marked TN. Inset map shows location of Flynn Creek impact structure and relative position of drill cores FC77-3 and FC67-3 on opposite sides of the central uplift (not shown). Asymmetrical outline [1, 2] is dashed.

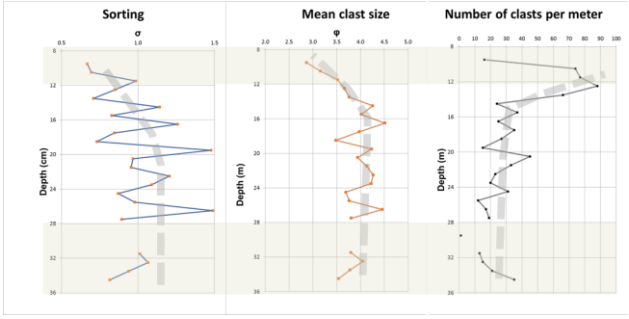

Figure 2. Main granulometric statistics from line logging of drill core FC77-3. Gray-shaded areas indicate where the cut-off grain size (top) as well as large blocks (bottom) affect the statistics [cf. 9]. Dashed line is our inferred trend line (i.e, not reflecting absolute values).

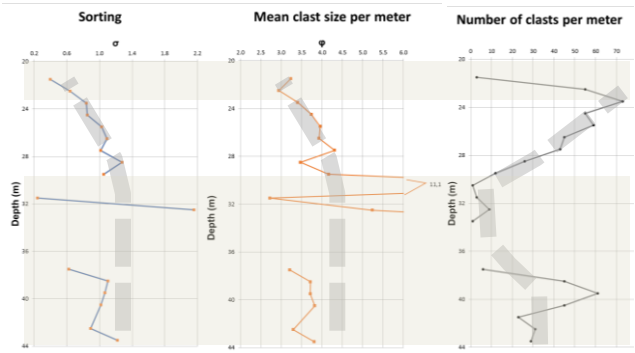

Figure 3. Main granulometric statistics from line logging of drill core FC67-3. Gray-shaded areas indicate where the cut-off grain size (top) as well as large blocks (bottom) affect the statistics [cf. 9]. Dashed line is our inferred trend line (i.e, not reflecting absolute values).

Figure 4. Representative lithological views of progressively fining upward core segments, 7.5 cm in length, from crater moat FC drill cores. From right to left: lower coarse breccia; finer upper breccia; fine upper breccia with clast size under the 5 mm cut-off grain size; and post-impact Chattanooga Shale.

EPSC Abstracts
Vol. 11, EPSC2017-998, 2017
European Planetary Science Congress 2017

Meteorite Atmospheric Entry Reproduced in Plasmatron II: Iron Oxidation State Change Probed by Xanes

G. Giuli (1), G.O. Lepore (2), L. Pittarello (3), S. McKibbin (4), S. Goderis (4), B. Soens (4), F. Bariselli (4,5), B.R. Barros Dias (5), F.L. Zavalan (5), T. Magin (5), Bernd Helber (5), and Ph. Claeys (4)
(1) University of Camerino, Via Gentile III da Varano, I-62032 Camerino, Italy, (2) CNR-IOM-OGG c/o ESRF, Avenue des Martyrs CS 40220 F-38043 Grenoble, France, (3) Department of Lithospheric Research, University of Vienna, Althanstraße 14, A-1090 Vienna, Austria, (4) Analytical, Environmental, and Geo-Chemistry (AMGC), Vrije Universiteit Brussel (VUB) Pleinlaan 2, B-1050 Brussels, Belgium, (5) von Karman Institute for Fluid Dynamics (VKI), Waterloosesteenweg 72, B-1640 Sint-Genesius-Rode, Belgium (email: gabriele.giuli@unicam.it)

Abstract

Heating experiments are one of the approaches used to investigate those changes experienced by meteoroids during their atmospheric entry. In this work, we are going to present the preliminary results from scanning electron microscopy and X-ray Adsorption Spectroscopy, in order to quantify the oxidation state of Fe produced in the VKI Plasmatron.

1. Introduction

Atmospheric entry of meteoroids is a complex process that involves melting, evaporation, and redox variations of the original material. Meteorites recovered on the ground are used for constraining the composition and the history of the parent bodies, but atmospheric entry can induce significant changes in microstructures and chemistry that may bias our interpretation. Ablation and heating effects are generally investigated by numerical modeling (e.g., [1]) or by heating experiments, which are however far from reaching the conditions experienced by meteoroids (e.g., [2,3]). Here we present preliminary results from scanning electron microscopy (SEM) and X-ray Adsorption Spectroscopy (XANES), aimed at determining the oxidation state of Fe, on material produced during the first experiments in the VKI Plasmatron. This instrument creates a steady state plasma flow up to 22 mbar pressure, over 10000 K temperature, with a potential heat flux of 16 MW/m^2, and is commonly used for testing spacecraft heat shields. It represents, therefore, a good approximation of the conditions encountered by any material during the atmospheric entry.

2. Methods

Cylinders of ca. 1 cm diameter and 2 cm length were drilled from a specimen of alkali basalt that was chosen as a terrestrial analogue for meteorites. Samples were jacketed in cork or graphite for two series of experiments. Several experimental conditions have been tested at the VKI, varying the pressure (15-220 mbar) and the exposure time (21-51s), keeping constant the heat flux to $3MW/m^2$. After the experiment, droplets of melt flowing over the sample holder and the sample itself (cut in two halves, normal to the flow) were analyzed with μ-XRF and SEM, equipped with EDS detector, at the VUB.

Fe K-edge X-ray Absorption Spectroscopy XANES and EXAFS data have been collected at beamline BM08 of the ESRF storage ring (Grenoble, F). Analysis of the pre-edge peak data has been done according to the method reported by [4] on the result of an ablation experiment and on a sample of the starting basalt ground to powder.

3. Results

The molten sample clearly shows a change in the bulk chemical composition, with respect to the original material, with a strong depletion in alkali and generally highly volatile elements and an apparent enrichment in refractory elements. Ejection of material is less obvious, but droplets of melt were observed to flow radially on the surface of the sample holder. At the transition between the melt coating, and the unaffected portion of the sample, melt spherules have formed.

Melt spherules have formed and represent the experimental analogue of ablation spherules from meteoroids. The melt exhibits schlieren and flow fabric. Tiny vesicles seem to be coated by iron oxides.

The XAS spectrum of the starting basalt displays values of the edge energy typical of trivalent Fe. As the starting material is a multiphase mixture, it is difficult to determine accurately the Fe oxidation state by means of the pre-edge peak centroid in the absence of constrains on the Fe content in the constituting phases. However, comparison of the pre-edge peak centroid with those of Fe model compounds provides a determination of the $Fe^{3+}/(Fe^{2+}+Fe^{3+})$ ratio close to 0.75±0.15. The edge energy of the melt sample is consistent with the presence of Fe^{2+}. Pre-edge peak data allow an accurate evaluation of a $Fe^{3+}/(Fe^{2+}+Fe^{3+})$ ratio close to 0.19±0.05.

4. Conclusions

Melting experiments with plasmatron offer a broad range of applications in planetary science, from investigation of meteorite fusion crust and micrometeorite formation to the evolution of impact ejecta. In these preliminary experiments, the change in bulk composition in the melt supports the hypothesis of alkali vaporization during atmospheric entry, based on studies of cosmic spherules (e.g., [5, 6]).

XAS data provide reliable determination of the Fe oxidation state. In this case, the starting material (with mostly trivalent Fe) upon melting has been reduced producing a glass with an $Fe^{3+}/(Fe^{2+}+Fe^{3+})$ ratio equal to 0.19±0.05. The iron reduction could be possibly caused by the extremely high temperature of the experiment. In order to obtain a complete characterization of the oxidation state changes due to atmospheric entry of extraterrestrial material, further analyses of the material produced in experiments performed using equilibrated ordinary chondrites (containing mostly divalent and metallic iron) as starting material are planned.

References

[1] Love S.G. and Brownlee D.E. 1991. Icarus 89:26-43.

[2] Greshake A. et al. 1998. Meteoritics & Planetary Science 33:267-290.

[3] Toppani A., et al. 2001. Meteoritics & Planetary Science 36:1377-1396.

[4] Wilke et al., 2001 American Mineralogist, 86, 714.730; Giuli et al., 2002, Geochimica et Cosmochimica Acta, 66, 4347-4353; Giuli et al., 2011, American mineralogist, 96, 631-636.

[5] Cordier C. et al. 2011. Geochimica et Cosmochimica Acta 75:5203-5218.

[6] Rudraswami N.G. et al. 2012. Geochimica et Cosmochimica Acta 99:110-127.